Ventral stress fibers induce plasma membrane deformation in human fibroblasts

Samuel J. Ghilardi, Mark S. Aronson, and Allyson E. Sgro*
Department of Biomedical Engineering and the Biological Design Center, Boston University, Boston, MA 02215

ABSTRACT **Interactions between the actin cytoskeleton and the plasma membrane are important in many eukaryotic cellular processes. During these processes, actin structures deform the cell membrane outward by applying forces parallel to the fiber's major axis (as in migration) or they deform the membrane inward by applying forces perpendicular to the fiber's major axis (as in the contractile ring during cytokinesis). Here we describe a novel actin–membrane interaction in human dermal myofibroblasts. When labeled with a cytosolic fluorophore, the myofibroblasts displayed prominent fluorescent structures on the ventral side of the cell. These structures are present in the cell membrane and colocalize with ventral actin stress fibers, suggesting that the stress fibers bend the membrane to form a "cytosolic pocket" that the fluorophores diffuse into, creating the observed structures. The existence of this pocket was confirmed by transmission electron microscopy. While dissolving the stress fibers, inhibiting fiber protein binding, or inhibiting myosin II binding of actin removed the observed pockets, modulating cellular contractility did not remove them. Taken together, our results illustrate a novel actin–membrane bending topology where the membrane is deformed outward rather than being pinched inward, resembling the topological inverse of the contractile ring found in cytokinesis.**

Monitoring Editor
Dennis Discher
University of Pennsylvania

Received: Mar 2, 2021
Revised: Jun 4, 2021
Accepted: Jun 22, 2021

INTRODUCTION

Critical cellular processes ranging from contraction (Lo *et al.*, 2000; Tee *et al.*, 2011; Zhou *et al.*, 2017) and migration (Cramer, 1997, 1999; Lo *et al.*, 2000; Zaman *et al.*, 2006) to proliferation (Wang *et al.*, 2000; Wang and Riechmann, 2007; Engler *et al.*, 2006; Levental *et al.*, 2009; Fu *et al.*, 2010) involve actin filaments (Cramer *et al.*, 1997; Pelham and Wang, 1997; Chen, 2008; Colombelli *et al.*, 2009; Wozniak and Chen, 2009; Martino *et al.*, 2018). In many cell types, including fibroblasts, actin filaments associate together with myosin proteins to form specialized actin stress fibers (Weber and Groeschel-Stewart, 1974; Verkhovsky and Borisy, 1993; Cramer *et al.*, 1997; Thoresen *et al.*, 2011) that provide mechanical integrity and generate contractile forces in the cell. As part of these processes, actin stress fibers interact with the cell's plasma membrane, most commonly at the end of the fiber through adapter proteins (such as talins or vinculin) at focal adhesions (Muguruma *et al.*, 1990; Calderwood *et al.*, 2003; Humphries *et al.*, 2007). These focal adhesion–stress fiber interactions are a common way to classify stress fibers, depending on whether the fiber is coupled to focal adhesions on both ends (ventral stress fiber), on one end (dorsal stress fiber), or not coupled to a focal adhesion (transverse arc) (Hotulainen and Lappalainen, 2006). In addition to the coupling of one or both ends of stress fibers to focal adhesions, there are also adapter proteins that couple the membrane to individual actin filaments along the length of the stress fiber, such as the ezrin/radixin/moesin (ERM) family of proteins (Arpin *et al.*, 1994; Turunen *et al.*, 1994; Nakamura *et al.*, 2000). Through these protein–membrane interactions, actin stress fibers deform the membrane at smaller structures such as focal adhesions (Abercrombie *et al.*, 1971; Medalia and Geiger, 2010). Besides stress fibers, actin structure–membrane interactions also include small structures such as filopodia, as well as larger projections like lamellipodia (Abercrombie *et al.*, 1970; Small and Celis, 1978; Svitkina, 2018).

To deform the plasma membrane, actin filaments apply force along their principal axis through actin polymerization (Wegner, 1976; Cortese *et al.*, 1989; Mogilner and Oster, 1996), while actin

This article was published online ahead of print in MBoC in Press (http://www.molbiolcell.org/cgi/doi/10.1091/mbc.E21-03-0096) on June 30, 2021.

*Address correspondence to: Allyson E. Sgro (asgro@bu.edu).

Abbreviations used: α-SMA, alpha smooth muscle actin; ATP, adenosine triphosphate; 2D, two dimensions; 3D, three dimensions; DMEM, Dulbecco's modified eagle medium; ERM, Ezrin/Radixin/Moesin; HDFs, human dermal fibroblasts; MLCP, myosin light chain kinase; NEAA, non-essential amino acids; PBS, phosphate buffered saline; PFA, paraformaldehyde; ROCK, Rho-associated protein kinase; TEM, transmission electron microscopy; TGF-β1, Transforming Growth Factor Beta 1.

stress fibers can also deform the membrane via myosin II contraction (Rüegg *et al.*, 2002; Giannone *et al.*, 2007; Vicente-Manzanares *et al.*, 2009; Craig *et al.*, 2012). As a result, during most membrane deformation events, actin structures generally deform the membrane parallel to the major axis of the fiber. A notable exception to this is during specialized membrane pinching events, such as the contractile ring in cytokinesis, where actin filaments assemble into a ring-like structure and contract the membrane inward, applying force perpendicular to the axis of the fiber, although it is unclear whether this is caused by myosin contraction in actin structures, actin filament polymerization, or a combination of the two (Mabuchi and Okuno, 1977; Pelham and Chang, 2002; Powell, 2005; Subramanian *et al.*, 2013). In larger structures such as lamellipodia, the arp2/3 complex allows for branching of actin filaments (Mullins *et al.*, 1997, 1998) and the generation of complex membrane contours (Machesky and Insall, 1998; Amann and Pollard, 2001; Suraneni *et al.*, 2012; Wu *et al.*, 2012), but each individual filament applies forces axially along the fiber. So far, no reported actin structure applies forces perpendicularly along the length of the fiber (as in the contractile ring) but deforms the membrane outward (as in filopodia or lamellipodia formation). Here, we report such a structure: an actin-induced membrane bending that occurs along the length of an actin stress fiber, generating a stable cytosolic pocket. We find that this pocket requires direct coupling of the fiber to the membrane, but once it is formed its stability is independent of active, myosin II–mediated fiber contraction.

RESULTS AND DISCUSSION

Novel fluorescent structures are observed in myofibroblasts labeled with a cytosolic fluorophore

After exposure to transforming growth factor beta (TGF-β1), fibroblasts transition to a myofibroblast phenotype (Moustakas and Stournaras, 1999; Hinz *et al.*, 2003, 2007), characterized by smooth muscle actin (α-SMA) expression (Desmoulière *et al.*, 1993), as well as an increase in stress fiber formation (Moustakas and Stournaras, 1999) and cellular contractility (Hinz *et al.*, 2001). We stimulated this transition in human dermal fibroblasts (HDFs) by culturing them with TGF-β1–containing media for 96 h, after which the HDFs expressed α-SMA (Supplemental Figure S1A) and developed prominent stress fibers, with some α-SMA incorporation (Supplemental Figure S1B). Surprisingly, during this transition, live HDFs loaded with cytosolic fluorescent dye developed fluorescent structures on the ventral side of the cells, as seen via spinning-disk confocal microscopy (Figure 1 and Supplemental Figure S2). These structures were not observed in cells grown on glass for 1 d in control media (Supplemental Figure S6A) but were seen in cells grown on glass in control media for 4 d (Supplemental Figure S6B), suggesting that these structures are not caused solely by TGF-β1 treatment. To test whether these structures were a dye-specific artifact, we generated HDF cell lines expressing either the fluorescent protein mNeonGreen or mScarlet-i and treated them with TGF-β1. Fluorescent structures were observed in both cell lines (Figure 1, B and C), suggesting that these observed fluorescent structures are not an artifact of a particular fluorophore. As a side observation, fluorescent puncta were observed in mScarlet-i–expressing cells but not in cells expressing mNeonGreen. It is possible that these puncta are similar to the mCherry aggregations previously observed in mouse neurons (Cai *et al.*, 2013) due to its mCherry lineage (Bindels *et al.*, 2017).

Observed fluorescent structures colocalize with ventral actin stress fibers

The observed fluorescent structures appear superficially similar to actin stress fibers, so we stained the cells with phalloidin to observe actin stress fibers and their potential relationship to these structures. The structures colocalized with actin stress fibers (Figure 2, A and C), leading us to hypothesize that the formation of these structures is related to stress fiber formation. Therefore, we decided to classify the type of stress fiber that colocalized with these ridges.

In two-dimensional (2D) cell culture, there are three kinds of actin stress fibers: ventral stress fibers, dorsal stress fibers, and transverse arcs (Burridge *et al.*, 1987; Burridge and Guilluy, 2016; Small *et al.*, 1998; Hotulainen and Lappalainen, 2006; Livne and Geiger, 2016). The different types of stress fibers can be distinguished by their association with focal adhesions. Specifically, ventral stress fibers are associated with focal adhesions on both ends of the fiber, dorsal stress fibers are associated with a focal adhesion on one end of the fiber, and transverse arcs are not associated with focal adhesions at all. We stained the cells with an anti–phospho-paxillin antibody to observe focal adhesions (Figure 2, B and D), which revealed that the majority of colocalized stress fibers started and ended at focal adhesions, identifying them as ventral stress fibers. In addition, the structures mainly appear on the bottom of the cell (Supplemental Movie S1). We also observed that the focal adhesions overlapped with the fluorescent structures (Figure 2, B and D, Supplemental Movie S1), suggesting that focal adhesions, as well as actin stress fibers, could play a role in fluorescent structure formation.

Fluorescent structures are formed by stress fiber–induced plasma membrane deformation along the fiber length

After determining that the observed structures colocalize with ventral actin stress fibers, we investigated potential mechanisms for how the stress fibers cause these structures. One possibility was that the dyes or fluorescent proteins were binding directly to stress fibers. However, neither the cytosolic Cell Explorer dye, mNeonGreen (Shaner *et al.*, 2013), nor mScarlet-i (Bindels *et al.*, 2017) has any reported intrinsic affinity for actin. Indeed, in the case of the fluorescent proteins in general, visualization of actin has previously necessitated their fusion to actin-binding moieties such as F-tractin or LifeAct (Schell *et al.*, 2001; Riedl *et al.*, 2008). These structures could instead be a type of invadosome such as invadopodia or podosome, both of which are actin-rich protrusions found on the ventral side of the cell (Murphy and Courtneidge, 2011; Eddy *et al.*, 2017; Masi *et al.*, 2020). However, staining for the protein TKS5, which is a marker for both invadopodia and podosomes (Courtneidge *et al.*, 2005; Burger *et al.*, 2011; Baik *et al.*, 2019; Chen *et al.*, 2019), revealed no colocalization with actin stress fibers or the fluorescent structures (Figure 3, A and B). In addition, invadopodia and podosome staining produces ring-like or punctate structures, not the long fiber-like structures observed in Figures 1 and 2. In a similar vein, these structures could be a type of filopodia. However, a stain for the filopodial marker fascin (Svitkina *et al.*, 2003; Vignjevic *et al.*, 2006) did not colocalize with either actin stress fibers or the fluorescent structures (Figure 3, C and D). Alternatively, the ventral stress fibers could be deforming the plasma membrane, creating a cytosolic "pocket" in the membrane around the stress fiber (Figure 4A). The fluorescent markers could then diffuse into this pocket, creating the fluorescent structures observed in Figure 1. In this hypothesis, the dye is not accumulating in the cytosolic pockets at higher concentrations relative to the rest of the cytosol. It is diffusing into the pockets only because they are an extension of the cytosol similar to the dye diffusing into membrane protrusions like filopodia (see Supplemental Movie S1 for an example of the dye intensity varying with the amount of cytosol in different *X*–*Y* slices through cells). As a corollary to this hypothesis, we would expect to see fluorescent structures around focal adhesions, as focal adhesions

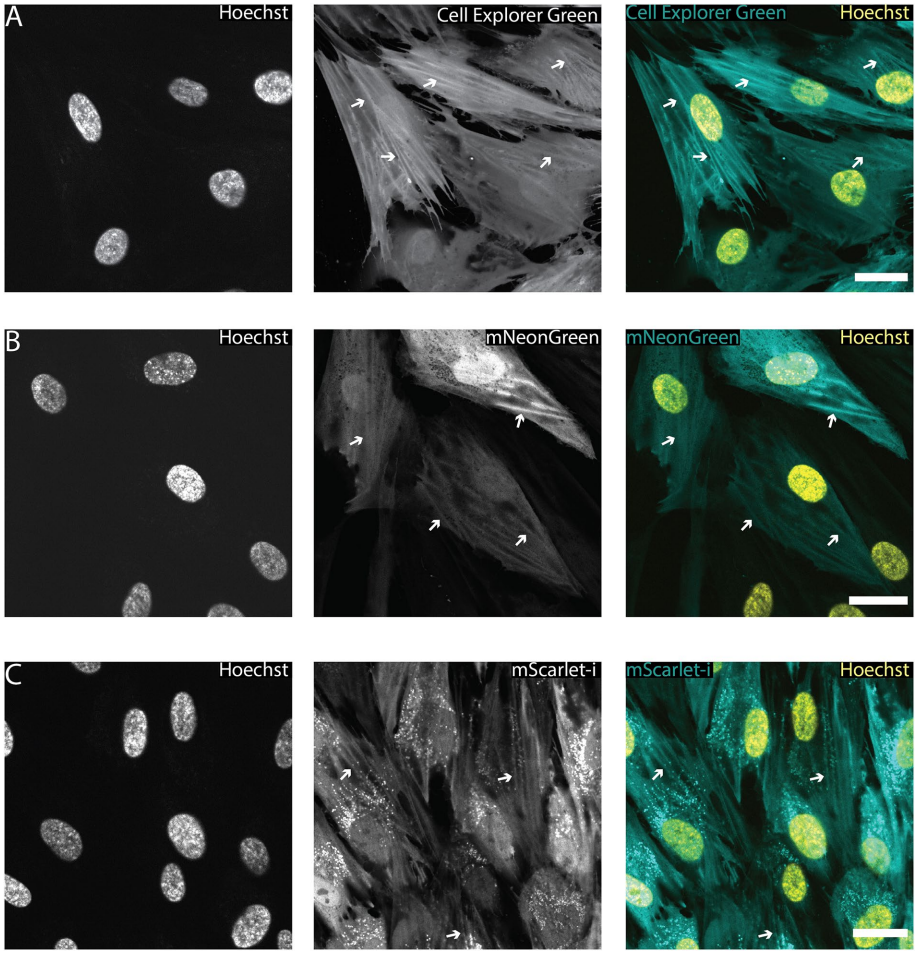

FIGURE 1: Fluorescent structures are visible in HDFs loaded with a cytosolic fluorophore. After 96 h of TGF-β1 treatment, HDFs transition into myofibroblasts (Supplemental Figure S1) and separately develop fluorescent structures on the ventral side of the cell (examples marked by white arrows). These ridges can be observed in naive cells labeled with (A) cell permeable dye or cells expressing fluorescent proteins such as (B) mNeonGreen or (C) mScarlet-i. Note that, at this magnification, fluorescent puncta can be seen in cells expressing either mScarlet-i or mCherry (Figure 6) but not mNeonGreen. There is also some visible bleedthrough from the blue (Hoechst) channel into the green (Cell Explorer/mNeonGreen) channel. (Scale bar = 25 μm.) Each experiment was conducted with three technical replicates in parallel, and a representative confocal slice from one well is shown.

also cause membrane deformation as seen via transmission electron microscopy (TEM) (Abercrombie *et al.*, 1970, 1971; Medalia and Geiger, 2010). An alternative hypothesis, where fluid flow from sodium pumps, rather than stress fibers (Li *et al.*, 2020), induced membrane deformation was tested, but sodium pump inhibition did not remove the observed fluorescent structures (Supplemental Figure S5).

To test this hypothesis, we estimated whether the forces and energy required to create these ridges are both possible and reasonable within the constraints of the cellular energy budget. To estimate the energy cost of membrane deformation by the ventral stress fiber, we started with calculating the free energy, G_{bend}, required to bend a membrane:

$$G_{bend}\left[h(x,y)\right]=\frac{K_b}{2}\int\left[\kappa_1(x,y)+\kappa_2(x,y)\right]^2 da \qquad (1)$$

where $h(x,y)$ is the height of the membrane at position (x,y) relative to some reference height, K_b is the membrane bending rigidity (typically on the order of 10–20 k_BT), κ_1 is the curvature of the membrane in the x dimension at position (x,y), κ_2 is the curvature of the membrane in the y dimension at position (x,y), and da is differential area. To simplify our calculations, we assumed that a fiber can be treated as a straight cylinder indenting a planar membrane (Figure 4B). This collapses the curvature consideration to one dimension, as all of the curvature along the y-axis will be the same at any given x (Figure 4C). This simplified our free energy equation calculation to Eq. 2:

$$G_{bend}\left[h(x,y)\right]=\frac{K_b * L}{2}\int\left[\kappa_1(x)\right]^2 dx \qquad (2)$$

where L is the length of the fiber cylinder. Curvature of a 1D line is calculated using Eq. 3:

$$\kappa(x)=\frac{\left|f''(x)\right|}{\left(1+f'(x)^2\right)^{3/2}} \qquad (3)$$

where $f(x)$ is the function describing the change in height of a line. We built some simple fitting equations to model this profile of the membrane around the fiber (see *Materials and Methods*). The range of free energy requirements fell into two regimes: when the center point of the fiber was modeled above the plane of the membrane and when the center point of the fiber was below the plane of the membrane. In the first regime, the free energy requirements were calculated using the assumption that the membrane bent directly around the fiber (Figure 4C, first two panels). The calculated energies fell in the range of 0–500 k_BT. In the second regime, along with bending around the fiber, parts of the membrane extending out past the fiber diameter were also simulated as bending (Figure 4C, last three panels). While the exact energy values depend on how these equations describe the membrane bending, we found that the estimates generally fell in the range of a few thousand k_BT. As a comparison point, the free energy of vesicle formation is ~500 k_BT, so the first regime of this membrane bending phenomenon is estimated to be on the same order of magnitude, while the second regime, the one that predicts the pocket that fluorescent molecules diffuse into (Figure 4C, final panel), falls no more than one order of magnitude above this known phenomenon. After examining the overall energy requirements, we then examined whether the actual energy budget required to induce this phenomenon was reasonable given the time frame and estimated energy requirement.

To see whether the energy of the membrane bending hypothesis fell within a reasonable energy budget of a fibroblast cell, we estimated the number of ATP molecules required to contract the stress fibers to cause sufficient bending in the membrane. While we recognize that the addition of actin filaments to a ventral stress fiber is a dynamic process, we assumed a static bundle of fibers for the purposes of this calculation. We started by assuming a range of possible radii for the stress fibers. We then calculated the number of

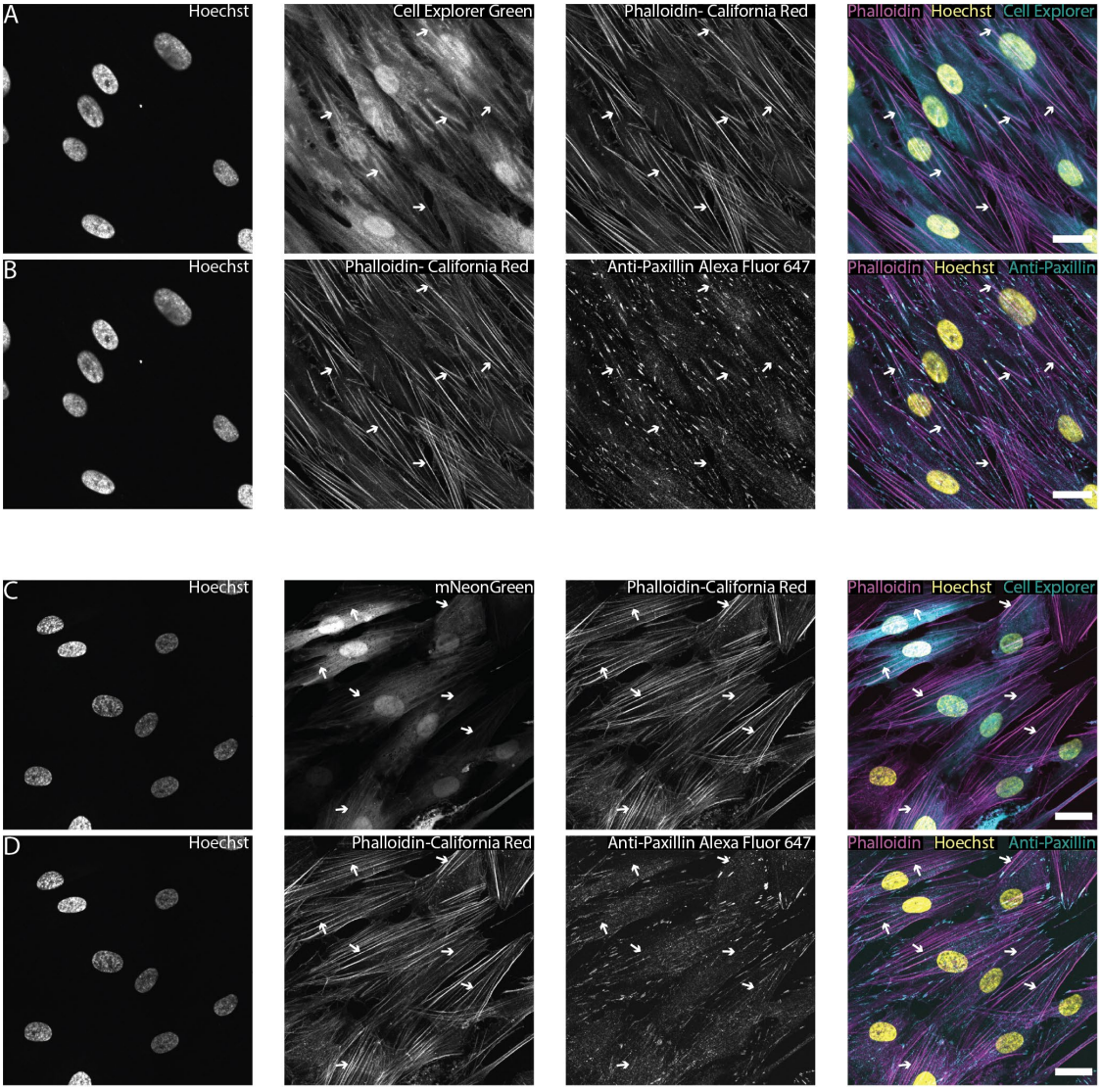

FIGURE 2: Fluorescent structures colocalize with ventral actin stress fibers. (A, B) Cells either stained with green Cell Explorer dye or constitutively expressing mNeonGreen (C, D) were fixed and stained with Hoechst (nuclei), phalloidin-California Red (actin), and an anti–phospho-paxillin primary antibody (focal adhesions) with an Alexa Fluor 647 secondary. The fluorescent structures (examples marked with white arrows) observed with either the (A) Cell Explorer dye or (C) mNeonGreen colocalize with phalloidin-stained stress fibers. The colocalized fibers have focal adhesions on both ends of the fiber (B, D), identifying them as ventral stress fibers. (Scale bar = 25 μm.) A and B and C and D are different channels for the same field of view. (Note: There is also some visible bleedthrough from the blue (Hoechst) channel into the green (Cell Explorer/mNeonGreen) channel. In addition, there is some accumulation of cytosolic fluorophore in the nucleus, as they all have a molecular weight below the 40 kDa nuclear diffusion limit [Wei *et al.*, 2003].) Each experiment was conducted with three technical replicates in parallel, and a representative confocal slice from one well is shown.

individual actin filaments in a given cross-section based on an actin filament radius of 8 nm. This allowed us to calculate the number of individual fibers of actin that needed to contract using Eq. 4:

$$N_{\text{actinfilaments}} = \frac{CSA_{\text{VSF}}}{CSA_{\text{actinfilament}}} = \frac{CSA_{\text{VSF}}}{8\text{nm}} \tag{4}$$

Actin polymers are contracted by myosin motors, whose step size has been estimated at 5 nm (Hundt *et al.*, 2016). It has also been measured that a myosin motor requires one ATP/step (Rief *et al.*, 2000). Using these estimates, we explored a range of ATP requirements for a variety of fiber radii and contraction lengths. Given the assumptions and estimates made, we calculated a linear relationship between energy requirement and how much length the fiber contracts, as shown by Eq. 5:

$$N_{\text{ATP}} = \frac{L_{\text{contraction}}}{L_{\text{stepsize}}} * N_{\text{ATP/step}} * N_{\text{actinfilaments}} \tag{5}$$

We calculated this relationship over a range of potential radii for the fibers (Figure 4D). Even for the largest estimate of fiber radius (250 nm), we calculated the energy requirement to be on the order of millions of ATP molecules.

To understand whether these values were reasonable, we compared the ATP requirement that we calculated with an estimate of the total ATP budget for a fibroblast cell. One calculation estimated fibroblast ATP production at 1 billion ATP/sec/cell (Flamholz *et al.*, 2014), putting a multiday formation of these membrane structures comfortably within the energy budget of the cell, ensuring that energy constraints were not a reason to rule out our hypothesis that

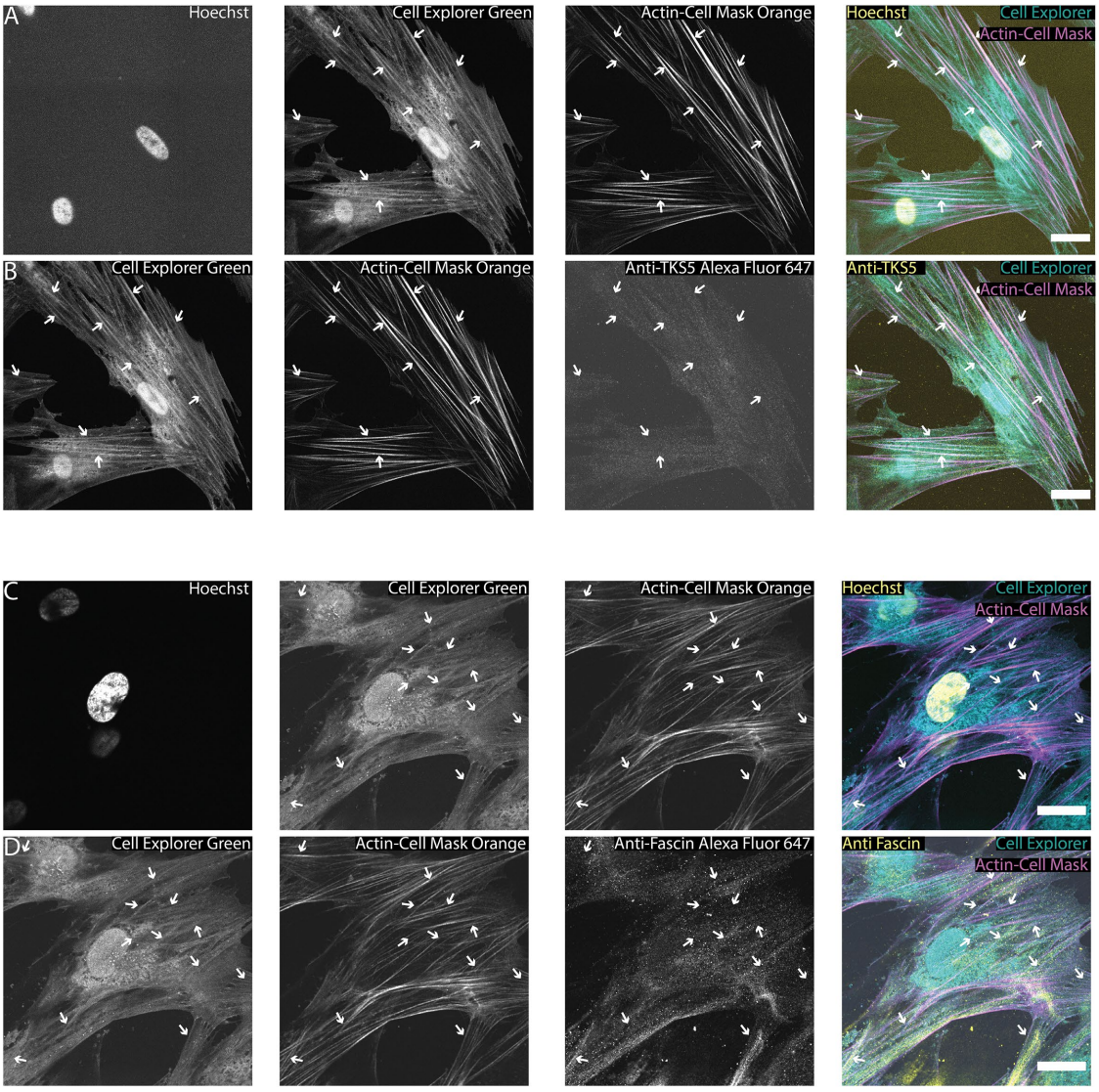

FIGURE 3: Neither invadopodial nor filopodial immunostaining colocalizes with observed fluorescent structures (A, B) HDFs stained with Hoechst (nuclei), Cell Explorer green (cytosol), Actin-Cell Mask Orange (actin), and anti-TKS5 antibody with an Alexa Fluor 647 secondary (invadopodia and podosomes). These cells have a TKS5 staining pattern similar to the negative control staining pattern provided by the manufacturer, which has no colocalization with actin stress fibers. (C, D) HDFs stained with Hoechst, Cell Explorer dye, Actin-Cell Mask Orange, and anti-Fascin antibody with an Alexa Fluor 647 secondary (filopodia) demonstrate no colocalization between the anti-Fascin antibodies and neither the actin cytoskeletion nor cytosolic pockets. (Note: There is also some visible bleedthrough from the blue (Hoechst) channel into the green (Cell Explorer) channel. In addition, there is some accumulation of cytosolic fluorophore in the nucleus, as they both have a molecular weight below the 40 kDa nuclear diffusion limit [Wei *et al.*, 2003].) Each experiment was conducted with three technical replicates in parallel, and a representative confocal slice from one well is shown. (Scale bar = 25 μm.)

the contraction of ventral stress fibers causes the formation of these structures.

Next, to test our membrane contour hypothesis experimentally, we stained the myofibroblast membranes with Green CellBrite Fix membrane dye (Figure 4E) and the actin stress fibers with phalloidin-California Red. If the cytosolic fluorescent structures were caused by actin stress fibers bending the membrane and forming a cytosolic pocket, we would expect to see similar fluorescent structures in the stained membrane that colocalize with actin stress fibers. Visualizing these stained cells using spinning-disk confocal microscopy, we clearly saw fluorescent structures in the cell membrane that colocalize in the *X*–*Y* plane with actin stress fibers, suggesting that the fluorescent structures involve the membrane as well as the cytosol, supporting our hypothesis. We confirmed these observations by directly visualizing the actin stress fibers and plasma membrane using TEM, with cells sectioned both parallel and perpendicular to the major axis of the cell (Figure 4, F and G and Supplemental Figure S4). In the cross-section perpendicular to the major axis of the cell (Figure 4F), curved cytosolic pockets ~1 μm in width and 500 nm in height can be seen protruding beneath the main cell body (white arrows). Inside this pocket, there is a 500-nm-diameter dark fibril haze, which looks similar to the ventral stress fibers taken in the images parallel to the major axis of the cell (Figure 4G, fiber marked by white arrows) and is consistent with other TEM

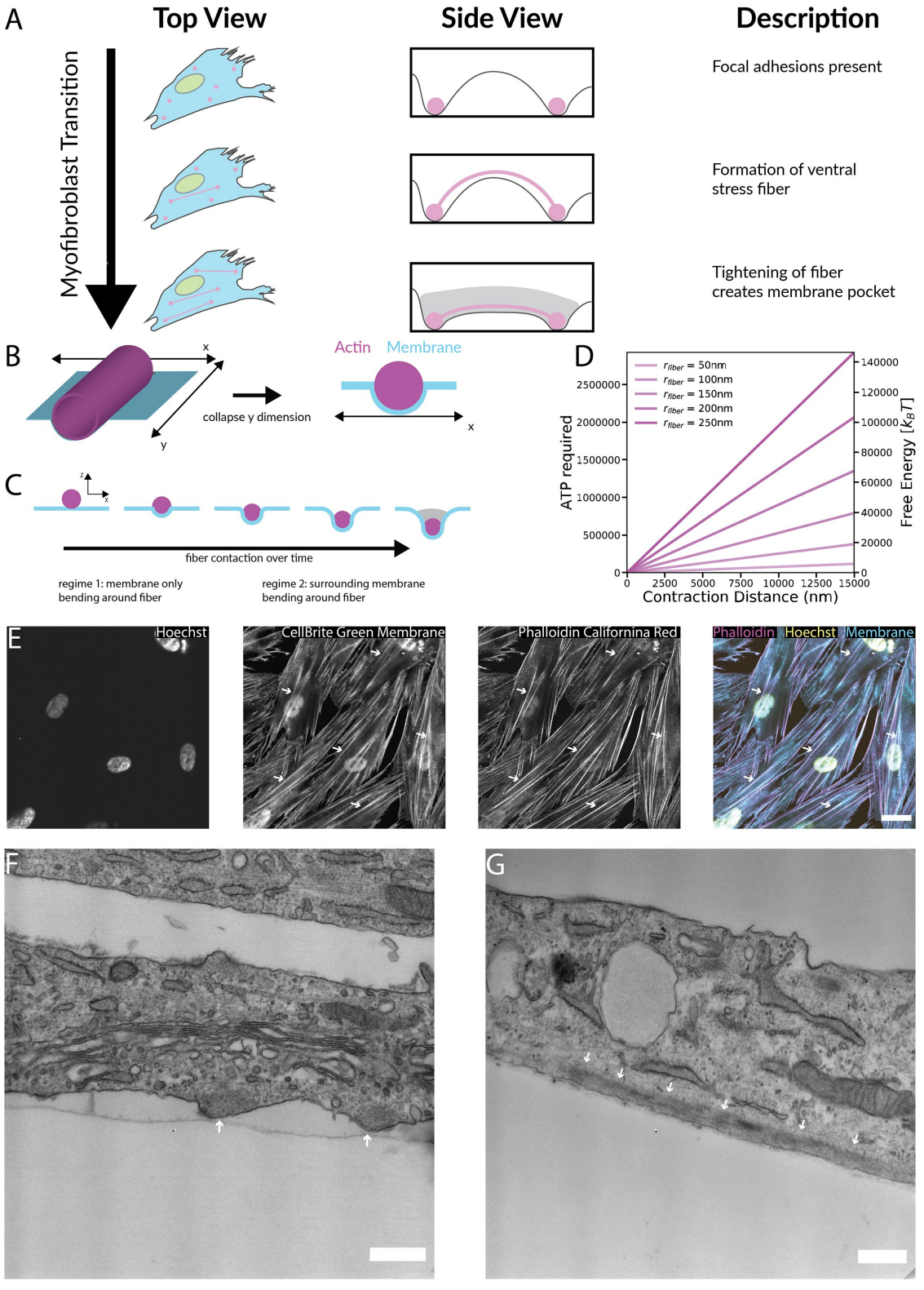

FIGURE 4: Actin stress fibers induce membrane deformation and cytosolic pocket formation, which can be visualized with cytosolic fluorophores. (A) Schematic of a proposed mechanism for the development of the fluorescent structures observed in Figure 1. As fibroblasts transition into myofibrobolasts, ventral actin stress fibers (magenta rods) originating from focal adhesions (magenta circles) deform the plasma membrane, creating cytosolic pockets (gray) for the fluorescent dye or proteins to diffuse into, leading to the observed fluorescent structures. (B) Model conceptualization of stress fiber–induced membrane deformation. The ventral stress fiber is modeled as a cylinder deforming a planar membrane. As the *y* dimension is uniform, the model is collapsed to one dimension. (C) Membrane deformation model used for membrane energy calculation. A stress fiber was modeled as lowering into a membrane, causing the membrane to curve. This fell into two regimes: one where the membrane is only deforming around the fiber and one

images of actin stress fibers (McNutt *et al.*, 1971; Perdue, 1973; Cramer *et al.*, 1997). Importantly, these cytosolic pockets do not look similar to TEM images of focal adhesions, lacking the distinct dark plaque on the cell membrane characteristic of focal adhesions seen both in our images (Supplemental Figure S3) and in the literature (Abercrombie *et al.*, 1970, 1971; Medalia and Geiger, 2010). Taken together, our imaging data demonstrate the existence of a cytosolic pocket in the membrane induced by actin stress fibers.

After observing that stress fibers induce membrane contouring, we investigated the structural linkage between ventral stress fibers and the plasma membrane. Paxillin staining (Figure 2, B and D) revealed that the ventral actin stress fibers are coupled to the plasma membrane via adapter proteins at focal adhesions. However, it is also possible for the actin cytoskeleton to bind the membrane at other points via other actin-binding proteins, such as ERM. In filopodia and membrane ruffles, ERM proteins bind the protruding actin to the membrane (Arpin *et al.*, 1994; Turunen *et al.*, 1994; Nakamura *et al.*, 2000). In epithelial cells undergoing an epithelial to mesenchymal transition induced by TGF-β1 treatment, ERM proteins colocalize with nascent actin stress fibers (Buckley *et al.*, 2010). To see whether ERM protein coupling is present in the observed fluorescent ridges, we stained for ERM proteins in our system, in addition to staining the cytosol with Cell Explorer green and actin stress fibers with California red (Figure 5A). In a separate experiment, we additionally stained for ERM proteins with an Alexa Fluor 514 secondary, the membrane with far red CellBrite Fix membrane dye, the cytosol using green Cell Explorer cytosolic dye, and actin stress fibers using phalloidin–Alexa Fluor 405 (Figure 5B). In both experiments, we observed colocalization between ERM proteins, actin stress fibers, membrane ridges, and the cytosolic pocket, suggesting that ERM proteins could be coupling the membrane to the actin stress fibers. Inhibiting ezrin–actin interactions using the ezrin inhibitor NSC66839 (Bulut *et al.*, 2012) caused the cytosolic pockets to disappear within 12 h, supporting our hypothesis that active ezrin–actin binding is necessary for membrane contouring (Figure 5, C and D). Interestingly, after ezrin inhibition, the actin stress fibers were still visible but exhibited a curved morphology (Figure 5D), suggesting that the membrane interactions might play a role in maintaining stress fiber persistence length, which could be an interesting topic to explore in future work.

Our evidence suggests that the membrane is directly coupled to stress fibers along the length of the fiber, so we next investigated the necessity of stress fiber structural integrity for membrane contouring by dissolving the stress fibers. We transfected myofibroblasts with an mCherry-paxillin fusion protein and loaded the cell with Cell Explorer dye and Cell Mask Far Red live cell actin stain to visualize the focal adhesions, cytosolic pockets, and the actin in living cells (Figure 6A). We then treated the cells with cytochalasin-D to disrupt the actin cytoskeleton network (Figure 6B). Cytochalasin-D dissolved ventral actin stress fibers along with their associated cytosolic pocket after 15 min of drug treatment, demonstrating that the physical membrane–stress fiber interaction is necessary for continued membrane contouring. In contrast, focal adhesions (marked by paxillin) are not dissolved by cytochalasin-D, and their corresponding cytosolic pocket remained intact after drug treatment, consistent with our hypothesis.

Actin-induced membrane contouring is not dependent on cellular contractility

Myofibroblasts have increased cellular contractility due to their expression of α-SMA (Desmoulière *et al.*, 1993) and the activation of RhoA GTPase (Tomasek *et al.*, 2002, 2006; Huang *et al.*, 2011; Midgley *et al.*, 2020). Cellular contractility derives from contraction of actin stress fibers by the molecular motor myosin II. In particular, the small GTPase RhoA and its downstream Rho-associated protein kinase (ROCK) play a key role in cellular contractility by modulating myosin II contraction via myosin light chain phosphatase (MLCP) inhibition (Ridley and Hall, 1992; Chrzanowska-Wodnicka and Burridge, 1996; Uehata *et al.*, 1997; Bhadriraju *et al.*, 2007). In our experiments, actin stress fiber deformation of the plasma membrane produces cytosolic pockets, so we investigated the role of actin stress fiber contractility in pocket stability. We stained the cytosol of myofibroblasts using Cell Explorer green and actin stress fibers using Cell Mask Orange or Deep Red actin stain (Figure 6C and Figure 7, A and C). We then treated HDFs with 10 nM of the phosphatase inhibitor calyculin A to increase cellular contractility (Tosuji, 1992; Suzuki and Itoh, 1993; Cho *et al.*, 2011) and 20 uM of the ROCK inhibitor Y-27632 to block RhoA-induced MLCP inhibition and decrease cellular contractility. Both calyculin A treatment over 15 min and Y-27632 treatment over 12 h resulted in actin stress fiber rearrangement as well as rearrangement of their corresponding cytosolic pockets (Figure 7 and Supplemental Movie S2). Critically, the stability and location of the cytosolic pockets mirrored the stability and location of the actin stress fibers, suggesting that once cytosolic pockets are formed, active stress fiber contraction is not needed to maintain membrane contouring. To further investigate the role of actin contractility in cytosolic pocket stability, we used the drug blebbistatin to directly inhibit myosin II–actin binding. This inhibition of myosin II–actin binding resulted in the disappearance of the cytosolic pockets

where parts of the membrane beyond the fiber are deforming. The energy requirement for bending the membrane was calculated across both regimes. (D) Results from stress fiber contraction calculation. In our proposed model, the contraction of the ventral stress fibers by myosin II motors drives the formation of the cytosolic pockets. Here, we consider the energy required for that contraction over a range of observed fiber radii (50–250 nm) and contraction distances (0–15,000 nm). The calculated ATP (left *y*-axis) and *kBT* equivalents (right *y*-axis) indicate that the proposed model is reasonable given the timeframe of cytosolic pocket formation. (E) Fluorescent structures can be observed in the plasma membrane after staining with Green-CellBrite fixable membrane dye (examples marked with white arrows). Like the cytosolic dyes in Figure 2, these fluorescent membrane structures colocalize with ventral actin stress fibers, supporting the hypothesis that ventral actin stress fibers play a role in the formation of the observed fluorescent structures. (Scale bar = 25 μm.) (F, G) TEM images of ventral actin stress fibers where (F) membrane deformation and (G) the thick ventral stress fibers can be directly observed (white arrows). The cytosolic pockets are distinct from focal adhesions that appear as a dark plaque near the membrane and exhibit sharp curvature on the edges (Supplemental Figures S3 and S4 and [Abercrombie *et al.*, 1970, 1971; Medalia and Geiger, 2010]). (Scale bar = 500 nm.) Note: The CellBrite dye also brightly stains the nuclear membrane, causing some nuclear bleedthrough from the green (CellBrite) channel into the red (phalloidin) channel. Figure 5B replicates this phalloidin/membrane staining with alternate dyes and minimal bleedthrough. Each experiment was conducted with three technical replicates in parallel, and a representative confocal slice from one well is shown.

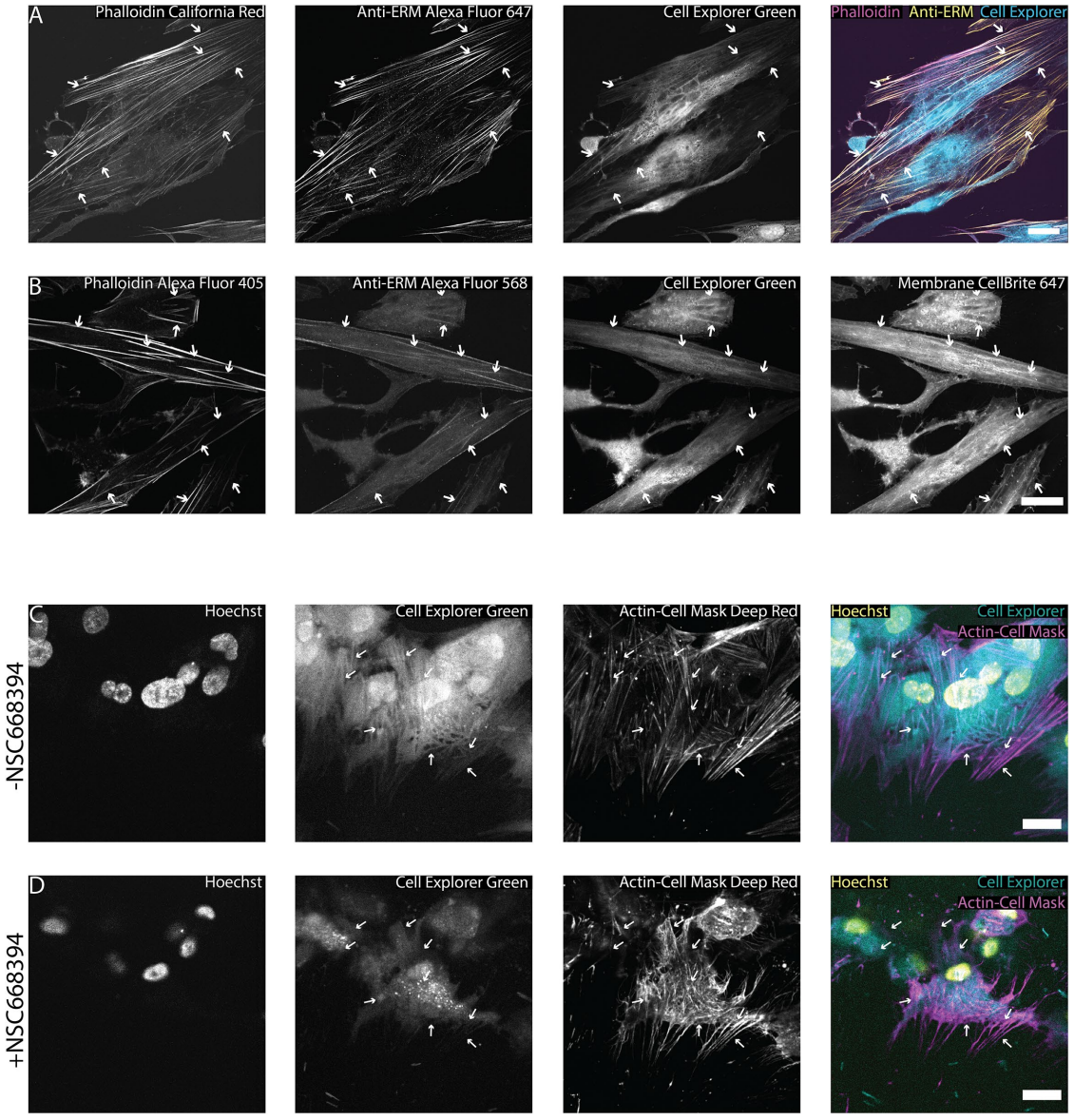

FIGURE 5: Direct coupling of stress fibers to the plasma membrane is necessary for membrane deformation. Immunofluorescence staining for ERM proteins reveals that ERM proteins colocalize with (A) stress fibers as well as (B) cytosolic and cell membrane pockets. (C) Before and (D) after images of cells treated with the ezrin inhibitor NSC66839. Treatment removes cytosolic pockets, but does not dissolve actin stress fibers, suggesting that physical coupling of the stress fiber to the membrane is necessary for membrane contouring. (Scale bar = 25 μm.) Each experiment was conducted with three technical replicates in parallel, and a representative confocal slice from one well is shown.

(Figure 6, C and D). This suggests that myosin-mediated actin interactions are necessary for actin stress fibers to contour the membrane. Taken together, these experiments that disrupt actin structures suggest that once cytosolic pockets are formed, only structural-stress fiber integrity (such as myosin II–actin binding), and not stress fiber contraction (mediated by ROCK induction of myosin II contraction), is necessary for membrane contouring. The necessity of fiber contraction for membrane ridge formation, but not membrane ridge maintenance, is tied to how ventral stress fibers are formed, which is typically from the fusion of mechanically tensed dorsal stress fibers and transverse arcs (Hotulainen and Lappalainen, 2006; Tojkander et al., 2015, 2018; Lee and Kumar, 2020). During this fusion process, myosin contractility increases and actin polymerization of the fused fibers decreases, leading to shortening of the nascent actin stress fiber, deformation of the plasma membrane in the *Z*-direction, and the formation of a cytosolic pocket. Ultimately, in cells with high contractility, the stress fiber is essentially parallel to the substrate (illustrated in Figure 4A and directly observed in Figure 4G). Ventral stress fibers are parallel to the cell substrate (Figure 4G; Hotulainen and Lappalainen, 2006), so contraction of stress fibers will shorten fiber length mainly in the *X*–*Y* plane and only minimally in the *Z* direction. Membrane deformation is mainly in the *Z* direction, meaning that contraction will have little effect on membrane deformation. However, fiber contraction will cause the fiber to move in the *X*–*Y* plane, and this was observed (Figure 7). It is also important to note that once formed, the length or turnover of individual actin filaments in the stress fiber do not necessarily impact the length or

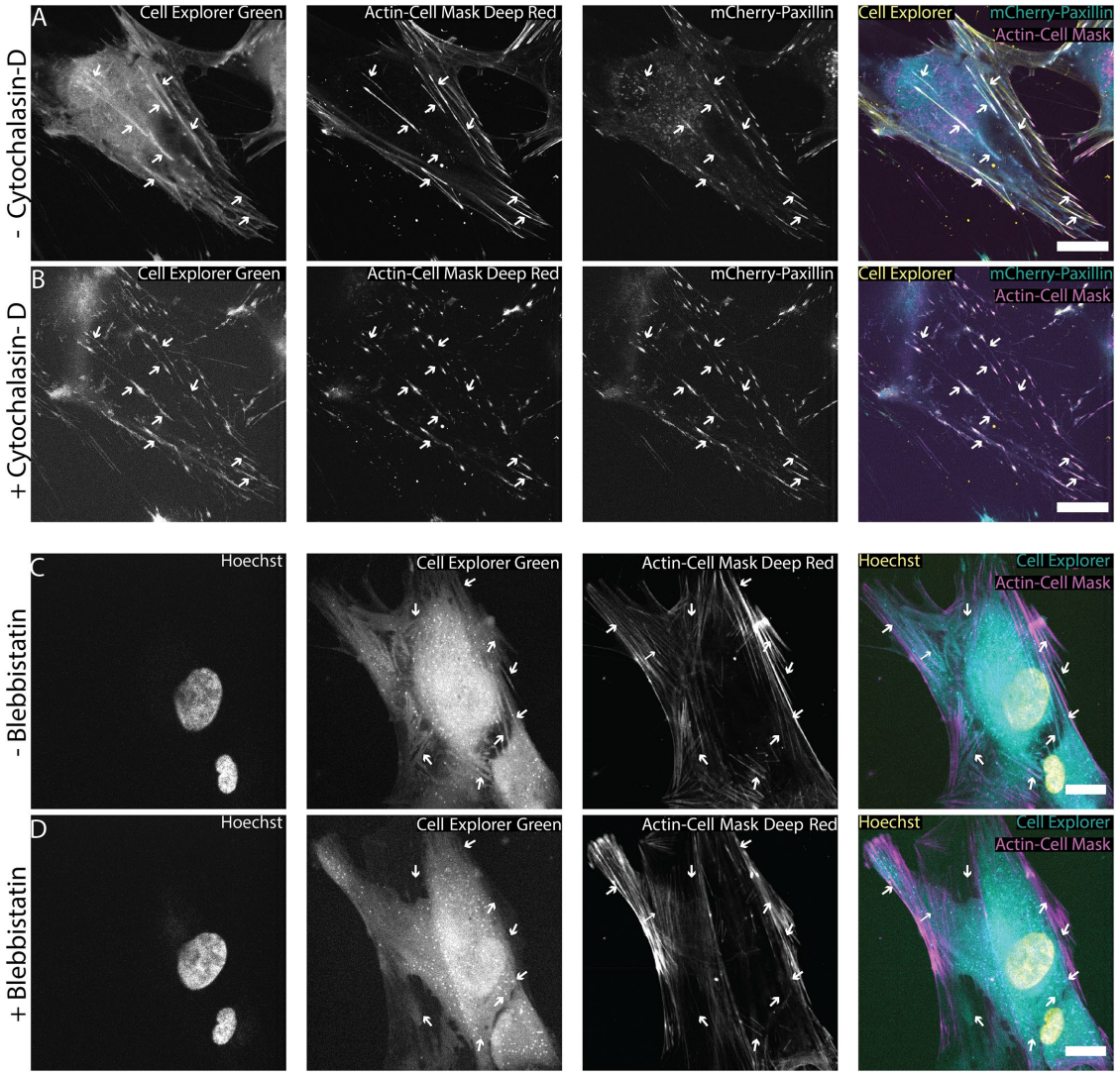

FIGURE 6: The structural integrity of actin stress fibers is required for membrane deformation. (A) Before and (B) after images of cells treated with cytochalasin-D. Cytochalasin-D treatment dissolved cytosolic pockets associated with stress fibers but not with focal adhesions, indicating that the physical structure of stress fibers is necessary for membrane deformation. (C) Before and (D) after images of cells treated with Blebbistatin. Blebbistatin treatment removed the observed cytosolic pockets but not the corresponding stress fibers, suggesting that once the membrane has been deformed, myosin–actin binding is necessary to maintain the cytosolic pocket. (Scale bar = 25 μm.) Each experiment was conducted with three technical replicates in parallel, and a representative confocal slice from one well is shown.

turnover of the stress fiber itself (Hotulainen and Lappalainen, 2006; Chapin *et al.*, 2012).

As a corollary to these observations, the process of stress fiber formation (and subsequent membrane deformation) can be observed in the HDFs grown without TGF-β1 as a control (Supplemental Figure S6). Even in the absence of TGF-β1, growing fibroblasts on a stiff substrate (such as plastic or glass) will promote an increase in stress fiber formation and cellular contractility (Solon *et al.*, 2007; Huang *et al.*, 2012; Gavara and Chadwick, 2016; Liu *et al.*, 2018). As a result, the Day 1 cells have few stress fibers and no membrane ridges (Supplemental Figure S6A). However, the Day 4 cells have prominent stress fibers (Supplemental Figure S6B) and appear to be in the middle of cytosolic pocket formation, as some cells display the fluorescent structures only at the ends of the stress fiber (double arrows), while others appear to have cytosolic pockets that run the length of the fiber (single arrows). However, while these data support the hypothesis that ventral stress fibers induce membrane deformation, the dynamics between ventral stress fiber formation and membrane deformation are not known and are a promising area for future study.

Contextualizing actin stress fiber–plasma membrane interactions

In this work, we have described a novel form of actin-induced membrane contouring where the actin stress fiber applies force perpendicular to the major axis of the fiber. This is in contrast to many actin–membrane interactions, such as those found in filopodia or lamellipodia, where force is applied parallel to the major axis of the fiber. In some ways, this new phenomenon is the topological inverse of the contractile ring found in cytokinesis. During cytokinesis, actin filaments form a contractile ring with the membrane on the outside of the ring. The contractile ring applies a centripetal force on the membrane, contracting the membrane inward, and eventually splitting the cell in half (Figure 8, left). In the ventral actin case described in this paper, the ventral actin stress fibers can be seen as an arc,

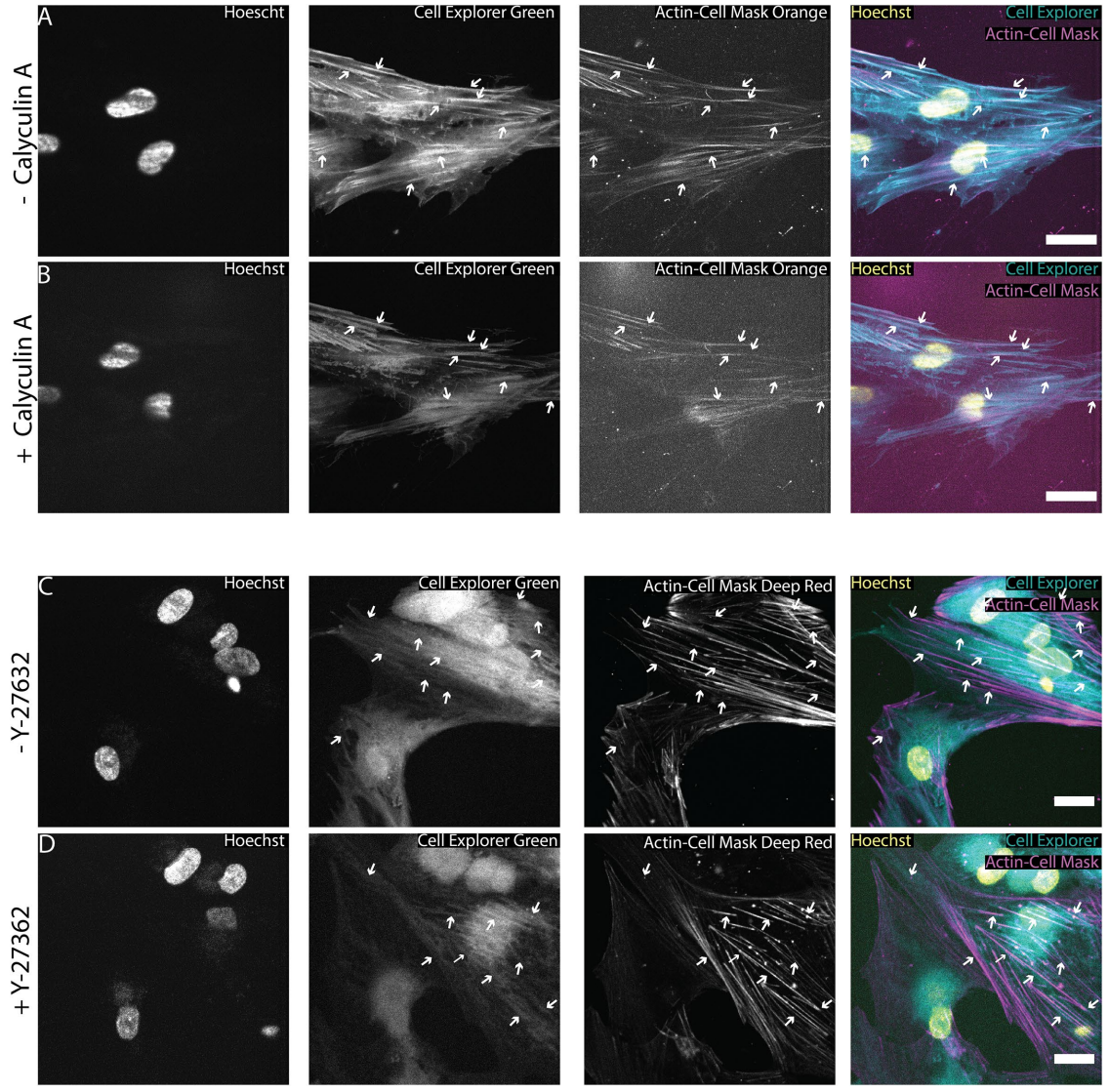

FIGURE 7: Active stress fiber contractility is not required to maintain membrane deformation. (A) Before and (B) after images of cells treated with calyculin A to increase cellular contractility. Calyculin A treatment did not alter the colocalization between cytosolic pockets and actin stress fibers. (C) Before and (D) after images of cells treated with Y-27632. Y-27632 treatment had no effect on the colocalization between the observed cytosolic pockets and actin stress fibers. Taken together, these two experiments suggest that once the membrane has been deformed, stress fiber contraction is not necessary to maintain membrane deformation. (Scale bar = 25 μm.) Each experiment was conducted with three technical replicates in parallel, and a representative confocal slice from one well is shown.

with the cell substrate serving as a chord bisecting a larger ring. Here, the membrane is on the inside of the fibers. The fibers then contract and apply the same centripetal force to the membrane, but because the membrane is on the inside of the fiber, it is stretched rather than contracted, forming the observed cytosolic pockets (Figure 8, right). There are a few key differences between these two processes. Namely, the actin ring found in cytokinesis is a specialized cytoskeletal structure found in dividing cells (Cao and Wang, 1990; Dean *et al.*, 2005; Zhou and Wang, 2008; Subramanian *et al.*, 2013; Chen *et al.*, 2017), whereas ventral actin stress fibers exist primarily in cells in interphase (Cramer *et al.*, 1997; Jones *et al.*, 2018; Vianay *et al.*, 2018; Li and Burridge, 2019). In addition, cytokinesis requires an active force in the actin ring to contract the membrane, through either myosin II contraction (Dean *et al.*, 2005; Zhou and Wang, 2008; Calvert *et al.*, 2011, actin treadmilling (Mendes Pinto *et al.*, 2012; Chew *et al.*, 2017), or a combination of both (Oelz *et al.*, 2015). In contrast, our experiments with Y-27632 and calyculin A suggest that once cytosolic pockets are observed, active cellular contractility is not needed to maintain membrane bending (Figure 7). The comparison between these two phenomena highlights both the structural and mechanical role actin structures play in the cell.

The mechanical environment of the cell likely plays a role in stress fiber formation and thus likely in the formation of the pockets that we identified here. There are a few critical differences between 2D cell culture and a 3D tissue environment in vivo, namely that in 2D there is artificial cell polarization and often stiffer substrates. A very stiff 2D substrate such as the glass used here does not accurately represent the native environment of dermal myofibroblasts, which are specialized to contract wounds closed (Li and Wang, 2011; Darby *et al.*, 2014), in vivo. Instead, we are observing artificially polarized actin–membrane interactions near the extreme end of myofibroblast contractility. Furthermore, in 2D culture, the cell

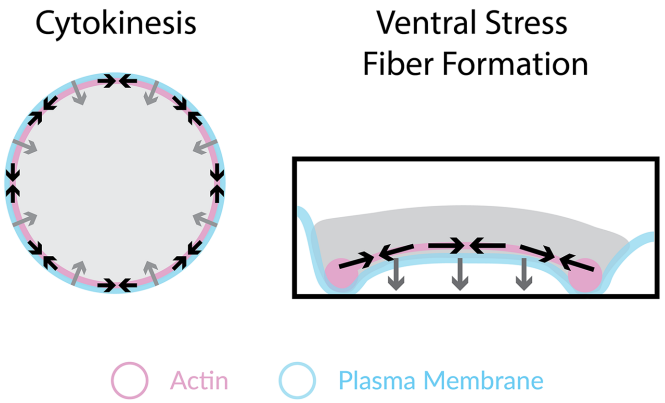

FIGURE 8: Contextualizing actin stress fiber–plasma membrane interactions. Schematics of the contractile ring in cytokinesis (left) and lateral membrane bending (right) demonstrating inverse topologies. In cytokinesis, an actin filament ring (magenta) contracts (black arrows) and applies a centripetal force (gray arrows) to the membrane (cyan), which is on the outside of the fiber, resulting in inward contraction of the membrane and ultimately membrane cleavage. In the novel ventral stress fiber–induced membrane bending, the ventral stress fibers can be viewed as an arc on a circle. In this case the membrane is on the inside of the fiber, and when these fibers contract (black arrows) and apply the centripetal force to the membrane (gray arrow), they deform the membrane and create cytosolic pockets.

can adhere to a substrate only on its ventral side, creating an artificial polarization where focal adhesions exist on only one side of the cell (Hotulainen and Lappalainen, 2006; Burridge and Wittchen, 2013), whereas in 3D focal adhesions exist on all sides of the cell (Deakin and Turner, 2011; Harunaga and Yamada, 2011; Kubow and Horwitz, 2011; Doyle *et al.*, 2015). In addition, these cells are grown on glass (Young's modulus on the order of 70 GPa [Seal *et al.*, 2001]), which is around 1000 times stiffer than native dermal tissue (Young's modulus on the order of 70 MPa [Geerligs *et al.*, 2011; Ní Annaidh *et al.*, 2012]). Therefore, it is possible that the environmental conditions in 2D that generate the high contractile forces necessary to laterally deform the membrane may not exist in a native 3D environment, and these structures are simply the product of 2D cell culture, adding to the list of evidence that 2D cell culture may not accurately replicate 3D in vivo tissue (Jensen and Teng, 2020). However, stress fibers do exist in 3D in vitro fibroblast culture (Mochitate *et al.*, 1991; Halliday and Tomasek, 1995; Pelham and Wang, 1999) and in 3D in vitro osteoblast culture (Zhu *et al.*, 2016; Nasello *et al.*, 2020) as well as in 3D in vivo tissues including endothelial cell tissues (Wong *et al.*, 1983; Franke *et al.*, 1984) and myofibroblasts in wounded dermal tissues (Gabbiani *et al.*, 1972; Grinnell, 1994; Mar *et al.*, 2001; Sandbo *et al.*, 2011). The existence of stress fibers in these in vivo contexts suggests that, under certain conditions, ventral actin stress fibers could potentially deform the plasma membrane in vivo as well, warranting further investigation into this phenomenon.

MATERIALS AND METHODS

Request a protocol through *Bio-protocol*.

Plasmid construction

pLentiCMV Puro Dest ERK-KTR was digested with *Bsr*GI to remove the ERK-KTR gene. The appropriate primers for each gene (see Table 1; plasmid sources are shown in Table 2) were used to generate PCR fragments of the gene and add 20–25 base homology arms to each end of the PCR fragment. The digested pLenti CMV Puro Dest vector and PCR fragment were assembled using NEB HiFi Assembly mix, and the mixture was transformed into NEBstable *Escherichia coli* and grown at 30°C overnight. Plasmids were sequence verified by Sanger Sequencing provided by Quintara Biosceince using the in-house CMV Forward (BP0002) and WPRE (BP0156) reverse primers.

Viral production

HEK293FT cells (passages 3–15) were plated at 90% confluency in a T-25 flask in HEK cell media (DMEM, 10% fetal bovine serum [FBS], 1× Glutamax, 1× non-essential amino acids [NEAA]). After 24 h, the flask was transfected with the pLenti plasmid and the packaging VSV-g and PSPAX-2 plasmids using Lipofectamine 3000, according to the manufacturer's protocol. After 12 h, the media in the dish was discarded and replaced. Media from the flask containing viral particles was collected 24 h later, replaced, and collected again 24 h later. The viral media was spun at 300 × *g* for 10 min to pellet any cells, and the supernatant was then passed through a 0.45 µm syringe filter. The resulting media was aliquoted in 500 µl tubes and stored at –80°C.

Neonatal HDF cell culture

Neonatal HDFs (passages 1–8) were cultured in fibroblast media (FGM media supplemented with an FGM-2 OneShot kit) in an

Name	Assembly construct	Sequence
mNeonGreen pLenti homology Fwd	pLenti CMV Puro mNeonGreen	GGAATTCTGCAGATATCAACAAGTTTGTACAGCCAC-CATGGTGAGCAAGGGCGAGGAG
mNeonGreen pLenti homology Rev	pLenti CMV Puro mNeonGreen	GATATCAACCACTTTGTACACTACTTGTACAGCTC-GTCCATGCC
mScarlet pLenti homology Fwd	pLenti CMV Puro mScarlet-i	ATATCAACAAGTTTGTCGACGCCACCATGGTGAG-CAAGGGCGAGGC
mScarlet pLenti homology Rev	pLenti CMV Puro mScarlet-i	TATCAACCACTTTGTACACGCGTTTACTTGTACAGCTC-GTCCATGCCG
mCherry pLenti homology Fwd	pLenti CMV Puro mCherry-Paxillin	ATCCGCTAGCGCTACCGGTCGCCACCATGGTGAG-CAAGGGCGAGGA
paxillin pLenti homolgy Rev	pLenti CMV Puro mCherry-Paxillin	GGATATCAACCACTTTGTACACGCGTCTAG-CAGAAGAGCTTGAGGAAGCAGT

TABLE 1: Primers for cloning.

Name	Source
pLentiCMV Puro Dest ERK-KTR	Addgene #59150
pLentiCMV Puro mNeonGreen	Synthesized
pLentiCMV Puro mScarlet-I	Synthesized
pLentiCMV Puro mCherry-Paxillin	Synthesized
PSPAX-2 viral packaging plasmid	Gift from the Ngo lab, Boston University
VSV-g viral envelope plasmid	Gift from the Ngo lab, Boston University

TABLE 2: Plasmids.

incubator at 37°C and 5% CO_2. Cells were passaged at 80–90% confluency, and media was changed every 48 h. To generate stably expressing pools of cells, fibroblasts were lifted from a flask by incubating the cells in 0.05% trypsin and then pelleted by centrifugation at 300 × *g* for 5 min. The cells were then resuspended in fresh fibroblast media and seeded in a 24-well plate at a concentration of 20,000 cells/well. Viral media (500 µl) and 500 µl of fibroblast media were then added to the well, and the dish was incubated at 37°C for 48 h. The media in the well was then changed to fibroblast media with 1 µg/ml puromycin to select for positively transduced cells. After 48 h, the cells were transferred to either a six-well dish for continued passaging or a new 24-well plate for experimentation.

Stress fiber induction

Fibroblasts were seeded at 20,000 cells/well in a glass-bottomed 24-well dish. After 24 h, stress fibers were induced by changing the cell media to a serum-free induction media (DMEM, 2% B-27, 10 ng/µl TGF-β1) that was refreshed every 48 h. Cells were used after 96 h of induction.

Confocal microscopy

After 96 h of induction, the cells were stained with various live cell stains according to the manufacturer's instructions, which generally involved diluting a stock solution 1000× (10,000× for Cell Mask Actin stain) in DMEM and incubating the cells for 15–30 min at 37°C and 5% CO_2. After staining, the cell media was changed to imaging media (Fluorobrite DMEM, 1% Glutamax, 1% OxyFluor). Cells were imaged on a Ti-2E Eclipse (Nikon Instruments) with a Dragonfly Spinning Disk confocal system controlled with Fusion software (Oxford Instruments) in a 37°C and 5% CO_2 stage top incubator (OKO Labs). Images were acquired on an iXon 888 Life EM-CCD camera (Oxford Instruments). Fluorescent dyes were imaged through a 405/488/561/647 dichroic mirror using the following excitation laser/emission filter combinations: Ex.405 nm-Em.445/50, Ex. 488 nm-Em. 515/30, Ex. 561 nm-Em. 590/60, Ex. 647- Em. 698/60. All staining and drug treatments were repeated in three separate wells, and a representative confocal slice was selected from each treatment for display in a figure. Wider field of view images (Supplemental Figure S2) were acquired in a 3 × 3 grid with 10% overlap and stitched using the stitching feature in Fusion (Preibisch *et al.*, 2009).

Inhibitor treatments

Cells were treated with the actin inhibitor cytochalasin-D (5 µM; Tocris), the ezrin inhibitor NSC668394 (50 µM; Calbiochem), Y27632 (25 µM; Hello Bio), calyculin A (10 nM; Cayman Chemical), Ouabain (30 nM; Tocris), and s-nitro-Blebbistatin 25 µM; Cayman Chemical). For cytochalasin-D and calyculin A treatment, an 18-slice Z-stack (140 nm step size) was acquired every minute for 5 min using a Plan Apochromatic 100× silicone oil immersion objective (Nikon; NA 1.35) as described above. After 5 min, a solution of cytochalasin-D dissolved in imaging media was injected into the well and the cells were imaged for another 15 min posttreatment. For NSC668394, Y27632, Ouabain, and S-nitro- Blebbistatin, cells were treated immediately before imaging and an 18-slice Z-stack (192.5 nm step size) was acquired every hour for 17 h using a Plan Apochromatic 40× air objective (Nikon; NA 0.95) and a 2× zoom lens (80× total magnification). Each drug treatment experiment was repeated in three separate wells, and multiple fields of view were collected per well.

Immunofluorescence

After 96 h of induction, cells were fixed in 4% paraformaldehyde (PFA) in phosphate-buffered saline (PBS) and permeabilized using 0.1% Triton-X. Nonspecific interactions were blocked using 10% normal goat serum in PBS. The cells were then incubated overnight with the primary antibody (anti-paxillin 1:50 and anti-ERM 1:100), washed in PBS, and then followed by incubation with the appropriate Alexa Fluor 647 secondary antibody (1:200) in 10% normal goat serum for 1 h at room temperature. In experiments where phalloidin or membrane stain was used, it was added after the secondary at 1:1000 in PBS and incubated for 30 min at room temperature. Cells were washed 3× in PBS and then imaged using the same parameters as previously described using a Plan Apochromatic 100× silicone oil immersion objective (Nikon) but at room temperature with no CO_2.

TEM

After 96 h of induction, cells were fixed in 2.5% PFA/glutaraldehyde in sodium cacodylate buffer for 1 h at room temperature. Cells were then washed with sodium cacodylate buffer 3× and stored at 4°C until imaged. Electron microscopy imaging, consultation, and services were performed in the HMS Electron Microscopy Facility on a TecnaiG2Spirit BioTwin microscope with a 2k AMT camera.

Western blotting

After stress fiber induction, HDFs were harvested from a 24-well dish by adding 100 µl of 4× LDS buffer and scraping the well using a 200 µl pipette tip. Samples were then diluted to 1× in Milliq H20 and incubated at 95°C for 10 min to denature the proteins. The denatured samples (10 µl) were then run on a 4–12% Bis-Tris PAGE gel in 1× MOPS buffer for 50 min at 150 V. Samples from the gel were transferred to a nitrocellulose membrane by using an IBlot2 Blotter (Invitrogen) and associated stack and applying a 20 V potential for 7 min. After transferring, the nitrocellulose membrane was incubated in 5% (wt/vol) nonfat dry milk in PBS + Tween for 1 h to block nonspecific interactions. Primary antibodies were added at the specified concentrations and incubated overnight at 4°C. After being washed in PBST, the membrane was incubated in 5% nonfat dry milk in PBST and the secondary antibody for 1 h at room temperature. The blot was then washed and imaged using the SuperSignalWest Pico solution and an iBright Western Blot Imager (Invitrogen).

Membrane bending energy calculations

All model calculations were carried out using a Python script in Spyder (version 4.1.5) using the NumPy (Harris *et al.*, 2020), Matplotlib (Hunter, 2007), and SciPy (Virtanen *et al.*, 2020) packages. To calculate membrane bending, the profile of the membrane wrapping around the fiber was defined as follows: until the midpoint of the fiber is level with the membrane, the membrane wraps directly

Name	Manufacturer	Lot
Cells		
Neonatal HDFs	Lonza (CC-2509)	0000490825, 0000490827, 0000493458
HEK293FT	ThermoFisher (R70007)	
Cell culture		
FBM media	Lonza (CC-3131)	0000849191, 0000914535
FGM-2 OneShot	Lonza (CC-4126)	0000851116, 0000885722, 0000923831
DMEM	Corning (MT10013CV)	10420009
Opti-MEM	Life Technologies (31985-062)	1897019
FluoroBrite DMEM	Life Technologies (a18967-01)	2120559
FBS	Life Technologies (16000044)	2103017RP
Pen-Strep	Life Technologies (16140-122)	2145104
B-27	Life Technologies (17504044)	2121033, 2193555
Glutamax	Life Technologies (35050-061)	2164667
Lipofectamine 3000	Thermo Fisher (L3000)	2177271
0.05% trypsin	Life Technologies (253000-054)	2120736
OxyFluor	Sigma-Aldrich (SAE0059)	SLCC2576
24-well glass-bottom dishes	Porvair Sciences (324042)	037505
24-well plastic dishes	Denville Scientific (T1024)	2018003
T-75 culture flasks	Fisher Scientific (156499)	161855
T-25 culture flasks	Denville Scientific (T1205)	2019001
Drugs		
Recombinant TGF-β1	R&D Systems (7754-BH)	DCPU0819111
Cytochalasin-D	Tocris (1233)	7A/207303
Y-27632	Hello Bio (HB2297)	E0807-1-4
NSC668394	Calbiochem (341216)	3434830
s-Nitro-Blebbistatin	Cayman Chemical Company (13891)	
Calyculin A	Cayman Chemical Company (19246)	0583516-3
Ouabain	Tocris (1076)	10A/250308
Immunofluorescence		
16% PFA	Thermo Fisher (PI28906)	UG287039
PBS	Life Technologies (7011-044)	2193380
Triton-X	Fisher (BP151)	176408
Normal goat serum	Southern Biotech (0060-01)	F3320-SD30B
Phalloidin Alexa Fluor 405	Thermo Fisher (A30104)	0529804-1
Phalloidin iFluor 488	Cayman Chemical (20549)	0593927
Phalloidin California Red	Cayman Chemical (20546)	0529804
Rabbit anti-paxillin antibody	Cell Signaling Technology (69363S)	1
Rabbit anti-ERM antibody	Cell Signaling Technology (3142T)	5
Rabbit anti-TKS5 (SH3 #1) antibody	Sigma-Aldrich (09-403)	
Rabbit anti-Fascin antibody	Proteintech Group (143841AP150UL)	
Goat anti-mouse Alexa Fluor 647 conjugate	Thermo Fisher (A21244)	2161043
Goat anti-rabbit Alexa Fluor 647 conjugate	Thermo Fisher (A21235)	2134003
Goat anti-rabbit Alexa Fluor 568 conjugate	Abcam (175471)	GR3189790-3
Hoechst 34580	Sigma-Aldrich (63493)	BCCB3802
Cell Explorer dye green	AAT Bioquest (22621)	2391532
CellBrite Fix 640 membrane dye	Biotium (30089T)	17C1115-1104173
CellBrite Fix 488 membrane dye	Biotium (30090A)	18C0118-1120003
Cell Mask Deep Red Actin Tracking Stain	Thermo Fisher (A57245)	2212430
Cell Mask Orange Actin Tracking Stain	Thermo Fisher (A57244)	2212429

TABLE 3: Sources for materials.

(*Continues*)

Name	Manufacturer	Lot
Plasmid cloning		
*Bsr*gI-HF	New England Biolabs (R3575)	10043043
*Dpn*I	New England Biolabs (R0176L)	10033040
2× Q5 PCR Master Mix	New England Biolabs (M0492S)	10047031
2× HiFi Assemby Master Mix	New England Biolabs (E2621)	
CutSmart Buffer	New England Biolabs (B7204S)	2441703
NEBstable Competent *E. coli*	New England Biolabs (C3040)	10061595
TEM prep		
Formaldehyde/glutaraldehyde 2.5%	Electron Microscopy Sciences (NC0620709)	200928-04
Sodium cacodylate buffer	Electron Microscopy Sciences (11650)	200811
12 mm coverslips	Fisher Scientific (C3040)	
Western blot		
NuPAGE LDS sample buffer (4×)	Invitrogen (NP0007)	2201446
NuPAGE 4–12% Bis-Tris protein gel	Invitrogen (NP0323BOX)	20121570
NuPage MOPS Running Buffer (20×)	Invitrogen (NP0001)	2166662
PBST (20×)	Bioworld (41620020-1)	L19061903MM
Novex iBlot 2 Nitrocellulose Transfer Stacks	Invitrogen (IB301031)	2NM191120-1
Nonfat dry milk	Stop & Shop (8826718269)	
Mouse anti–α-SMA antibody	Santa Cruz Biotechnology (sc-32251)	F0319
Mouse anti-GAPDH antibody	Santa Cruz Biotechnology (sc-32233)	E219
Goat anti-mouse HRP antibody	Invitrogen (G21040)	
SuperSignalWest Pico PLUS Chemiluminescent Substrate	Thermo Scientific (34577)	SI255887

TABLE 3: Sources for materials. Continued

around the fiber using a square root function. As the midpoint of the fiber dips below the level of the membrane, parts of the membrane to either side begin to bend. This is modeled by fitting hyperbolic curves that start at the *y* value at the midpoint of the fiber and have a length half the distance from the fiber midpoint to the resting level of the membrane. After the profile of the membrane has been defined, the curvature at each point is calculated using the derivative function from the SciPy package. The bending energy equation is applied for each point of curvature and summed over the whole stretch of membrane modeled to get the total bending energy. Code is available online at https://github.com/sgrolab/ventralsfpaper.

Sources and other details on materials used in this research are shown in Table 3.

ACKNOWLEDGMENTS

We thank Emily Mace, John Ngo, and Emily Hager for their critical review of our manuscript and helpful comments. This work was supported by National Institutes of Health (National Institute of General Medical Sciences) Grant R35 GM133616 to A.E.S. and a Burroughs Wellcome Fund Career Award at the Scientific Interface to A.E.S. M.S.A. was supported by a Multicellular Design Program fellowship from the Rajen Kilachand Fund for Integrated Life Sciences and Engineering. Electron microscopy imaging, consultation, and services were performed in the Harvard Medical School Electron Microscopy Facility.

REFERENCES

Abercrombie M, Heaysman JEM, Pegrum SM (1970). The locomotion of fibroblasts in culture I. Movements of the leading edge. Exp Cell Res 59, 393–398.

Abercrombie M, Heaysman JEM, Pegrum SM (1971). The locomotion of fibroblasts in culture: IV. Electron microscopy of the leading lamella. Exp Cell Res 67, 359–367.

Amann KJ, Pollard TD (2001). Direct real-time observation of actin filament branching mediated by Arp2/3 complex using total internal reflection fluorescence microscopy. Proc Natl Acad Sci USA 98, 15009–15013.

Arpin M, Algrain M, Louvard D (1994). Membrane-actin microfilament connections: an increasing diversity of players related to band 4.1. Curr Opin Cell Biol 6, 136–141.

Baik M, French B, Chen YC, Byers JT, Chen KT, French SW, Díaz B (2019). Identification of invadopodia by TKS5 staining in human cancer lines and patient tumor samples. MethodsX 6, 718–726.

Bhadriraju K, Yang M, Alom Ruiz S, Pirone D, Tan J, Chen CS (2007). Activation of ROCK by RhoA is regulated by cell adhesion, shape, and cytoskeletal tension. Exp Cell Res 313, 3616–3623.

Bindels DS, Haarbosch L, van Weeren L, Postma M, Wiese KE, Mastop M, Aumonier S, Gotthard G, Royant A, Hink MA, Gadella TWJ (2017). mScarlet: a bright monomeric red fluorescent protein for cellular imaging. Nat Methods 14, 53–56.

Buckley ST, Medina C, Kasper M, Ehrhardt C (2010). Interplay between RAGE, CD44, and focal adhesion molecules in epithelial-mesenchymal transition of alveolar epithelial cells. Am J Physiol Lung Cell Mol Physiol 300, L548–L559.

Bulut G, Hong SH, Chen K, Beauchamp EM, Rahim S, Kosturko GW, Glasgow E, Dakshanamurthy S, Lee HS, Daar I, *et al.* (2012). Small molecule inhibitors of ezrin inhibit the invasive phenotype of osteosarcoma cells. Oncogene 31, 269–281.

Burger KL, Davis AL, Isom S, Mishra N, Seals DF (2011). The podosome marker protein Tks5 regulates macrophage invasive behavior. Cytoskeleton 68, 694–711.
Burridge K, Guilluy C (2016). Focal adhesions, stress fibers and mechanical tension. Exp Cell Res 343, 14–20.
Burridge K, Molony L, Kelly T (1987). Adhesion plaques: sites of transmembrane interaction between the extracellular matrix and the actin cytoskeleton. J Cell Sci Suppl 8, 211–219.
Burridge K, Wittchen ES (2013). The tension mounts: stress fibers as force-generating mechanotransducers. J Cell Biol 200, 9–19.
Cai D, Cohen KB, Luo T, Lichtman JW, Sanes JR (2013). Improved tools for the Brainbow toolbox. Nat Methods 10, 540–547.
Calderwood DA, Fujioka Y, Pereda JMD, García-Alvarez B, Nakamoto T, Margolis B, McGlade CJ, Liddington RC, Ginsberg MH (2003). Integrin β cytoplasmic domain interactions with phosphotyrosine-binding domains: a structural prototype for diversity in integrin signaling. Proc Natl Acad Sci USA 100, 2272–2277.
Calvert MEK, Wright GD, Leong FY, Chiam KH, Chen Y, Jedd G, Balasubramanian MK (2011). Myosin concentration underlies cell size–dependent scalability of actomyosin ring constriction. J Cell Biol 195, 799–813.
Cao LG, Wang YL (1990). Mechanism of the formation of contractile ring in dividing cultured animal cells. II. Cortical movement of microinjected actin filaments. J Cell Biol 111, 1905–1911.
Chapin L, Blankman E, Smith M, Shiu YT, Beckerle M (2012). Lateral communication between stress fiber sarcomeres facilitates a local remodeling response. Biophys J 103, 2082–2092.
Chen A, Arora PD, McCulloch CA, Wilde A (2017). Cytokinesis requires localized β-actin filament production by an actin isoform specific nucleator. Nat Commun 8, 1530.
Chen CS (2008). Mechanotransduction—a field pulling together? J Cell Sci 121, 3285.
Chen YC, Baik M, Byers JT, Chen KT, French SW, Díaz B (2019). TKS5-positive invadopodia-like structures in human tumor surgical specimens. Exp Mol Pathol 106, 17–26.
Chew TG, Huang J, Palani S, Sommese R, Kamnev A, Hatano T, Gu Y, Oliferenko S, Sivaramakrishnan S, Balasubramanian MK (2017). Actin turnover maintains actin filament homeostasis during cytokinetic ring contraction. J Cell Biol 216, 2657–2667.
Cho YE, Ahn DS, Morgan KG, Lee YH (2011). Enhanced contractility and myosin phosphorylation induced by Ca2+-independent MLCK activity in hypertensive rats. Cardiovasc Res 91, 162–170.
Chrzanowska-Wodnicka M, Burridge K (1996). Rho-stimulated contractility drives the formation of stress fibers and focal adhesions. J Cell Biol 133, 1403–1415.
Colombelli J, Besser A, Kress H, Reynaud EG, Girard P, Caussinus E, Haselmann U, Small JV, Schwarz US, Stelzer EHK (2009). Mechanosensing in actin stress fibers revealed by a close correlation between force and protein localization. J Cell Sci 122, 1928.
Cortese JD, Schwab B, Frieden C, Elson EL (1989). Actin polymerization induces a shape change in actin-containing vesicles. Proc Natl Acad Sci USA 86, 5773–5777.
Courtneidge SA, Azucena EF, Pass I, Seals DF, Tesfay L (2005). The SRC substrate Tks5, podosomes (invadopodia), and cancer cell invasion. Cold Spring Harb Symp Quant Biol 70, 167–171.
Craig E, Van Goor D, Forscher P, Mogilner A (2012). Membrane tension, myosin force, and actin turnover maintain actin treadmill in the nerve growth cone. Biophys J 102, 1503–1513.
Cramer LP (1999). Organization and polarity of actin filament networks in cells: implications for the mechanism of myosin-based cell motility. Biochem Soc Symp 65, 173–205.
Cramer LP, Siebert M, Mitchison TJ (1997). Identification of novel graded polarity actin filament bundles in locomoting heart fibroblasts: implications for the generation of motile force. J Cell Biol 136, 1287–1305.
Darby IA, Laverdet B, Bonté F, Desmoulière A (2014). Fibroblasts and myofibroblasts in wound healing. Clin Cosmet Investig Dermatol 7, 301–311.
Deakin NO, Turner CE (2011). Distinct roles for paxillin and Hic-5 in regulating breast cancer cell morphology, invasion, and metastasis. Mol Biol Cell 22, 327–341.
Dean SO, Rogers SL, Stuurman N, Vale RD, Spudich JA (2005). Distinct pathways control recruitment and maintenance of myosin II at the cleavage furrow during cytokinesis. Proc Natl Acad Sci USA 102, 13473–13478.
Desmoulière A, Geinoz A, Gabbiani F, Gabbiani G (1993). Transforming growth factor-beta 1 induces alpha-smooth muscle actin expression in granulation tissue myofibroblasts and in quiescent and growing cultured fibroblasts. J Cell Biol 122, 103–111.
Doyle AD, Carvajal N, Jin A, Matsumoto K, Yamada KM (2015). Local 3D matrix microenvironment regulates cell migration through spatiotemporal dynamics of contractility-dependent adhesions. Nat Commun 6, 8720.
Eddy RJ, Weidmann MD, Sharma VP, Condeelis JS (2017). Tumor cell invadopodia: invasive protrusions that orchestrate metastasis. Trends Cell Biol 27, 595–607.
Engler AJ, Sen S, Sweeney HL, Discher DE (2006). Matrix elasticity directs stem cell lineage specification. Cell 126, 677–689.
Flamholz A, Phillips R, Milo R (2014). The quantified cell. Mol Biol Cell 25, 3497–3500.
Franke RP, Gräfe M, Schnittler H, Seiffge D, Mittermayer C, Drenckhahn D (1984). Induction of human vascular endothelial stress fibres by fluid shear stress. Nature 307, 648–649.
Fu J, Wang YK, Yang MT, Desai RA, Yu X, Liu Z, Chen CS (2010). Mechanical regulation of cell function with geometrically modulated elastomeric substrates. Nat Methods 7, 733–736.
Gabbiani G, Hirschel BJ, Ryan GB, Statkov PR, Majno G (1972). Granulation tissue as a contractile organ a study of structure and function. J Exp Med 135, 719–734.
Gavara N, Chadwick RS (2016). Relationship between cell stiffness and stress fiber amount, assessed by simultaneous atomic force microscopy and live-cell fluorescence imaging. Biomech Model Mechanobiol 15, 511–523.
Geerligs M, van Breemen L, Peters G, Ackermans P, Baaijens F, Oomens C (2011). In vitro indentation to determine the mechanical properties of epidermis. J Biomech 44, 1176–1181.
Giannone G, Dubin-Thaler BJ, Rossier O, Cai Y, Chaga O, Jiang G, Beaver W, Döbereiner HG, Freund Y, Borisy G, Sheetz MP (2007). Lamellipodial actin mechanically links myosin activity with adhesion-site formation. Cell 128, 561–575.
Grinnell F (1994). Fibroblasts, myofibroblasts, and wound contraction. J Cell Biol 124, 401–404.
Halliday NL, Tomasek JJ (1995). Mechanical properties of the extracellular matrix influence fibronectin fibril assembly in vtro. Exp Cell Res 217, 109–117.
Harris CR, Millman KJ, van der Walt SJ, Gommers R, Virtanen P, Cournapeau D, Wieser E, Taylor J, Berg S, Smith NJ, *et al*. (2020). Array programming with NumPy. Nature 585, 357–362.
Harunaga JS, Yamada KM (2011). Cell-matrix adhesions in 3D. Matrix Biol 30, 363–368.
Hinz B, Celetta G, Tomasek JJ, Gabbiani G, Chaponnier C (2001). Alpha-smooth muscle actin expression upregulates fibroblast contractile activity. Mol Biol Cell 12, 2730–2741.
Hinz B, Dugina V, Ballestrem C, Wehrle-Haller B, Chaponnier C (2003). α-Smooth muscle actin is crucial for focal adhesion maturation in myofibroblasts. Mol Biol Cell 14, 2508–2519.
Hinz B, Phan SH, Thannickal VJ, Galli A, Bochaton-Piallat ML, Gabbiani G (2007). The myofibroblast: one function, multiple origins. Am J Pathol 170, 1807–1816.
Hotulainen P, Lappalainen P (2006). Stress fibers are generated by two distinct actin assembly mechanisms in motile cells. J Cell Biol 173, 383–394.
Huang X, Gai Y, Yang N, Lu B, Samuel CS, Thannickal VJ, Zhou Y (2011). Relaxin regulates myofibroblast contractility and protects against lung fibrosis. Am J Pathol 179, 2751–2765.
Huang X, Yang N, Fiore VF, Barker TH, Sun Y, Morris SW, Ding Q, Thannickal VJ, Zhou Y (2012). Matrix stiffness–induced myofibroblast differentiation is mediated by intrinsic mechanotransduction. Am J Respir Cell Mol Biol 47, 340–348.
Humphries JD, Wang P, Streuli C, Geiger B, Humphries MJ, Ballestrem C (2007). Vinculin controls focal adhesion formation by direct interactions with talin and actin. J Cell Biol 179, 1043–1057.
Hundt N, Steffen W, Pathan-Chhatbar S, Taft MH, Manstein DJ (2016). Load-dependent modulation of non-muscle myosin-2A function by tropomyosin 4.2. Sci Rep 6, 20554.
Hunter JD (2007). Matplotlib: a 2D graphics environment. Comput Sci Eng 9, 90–95.
Jensen C, Teng Y (2020). Is it time to start transitioning from 2D to 3D cell culture? Front Mol Biosci 7, 33.
Jones MC, Askari JA, Humphries JD, Humphries MJ (2018). Cell adhesion is regulated by CDK1 during the cell cycle. J Cell Biol 217, 3203–3218.
Kubow KE, Horwitz AR (2011). Reducing background fluorescence reveals adhesions in 3D matrices. Nat Cell Biol 13, 3–5.

Lee S, Kumar S (2016). Actomyosin stress fiber mechanosensing in 2D and 3D. F1000Research 5, doi:10.12688/f1000research.8800.1.
Lee S, Kumar S (2020). Cofilin is required for polarization of tension in stress fiber networks during migration. J Cell Sci 133, jcs243873.
Levental KR, Yu H, Kass L, Lakins JN, Egeblad M, Erler JT, Fong SFT, Csiszar K, Giaccia A, Weninger W, *et al.* (2009). Matrix crosslinking forces tumor progression by enhancing integrin signaling. Cell 139, 891–906
Li B, Wang JHC (2011). Fibroblasts and myofibroblasts in wound healing: force generation and measurement. J Tissue Viability 20, 108–120.
Li Y, Burridge K (2019). Cell-cycle-dependent regulation of cell adhesions: adhering to the schedule. BioEssays 41, 1800165.
Li Y, Konstantopoulos K, Zhao R, Mori Y, Sun SX (2020). The importance of water and hydraulic pressure in cell dynamics. J Cell Sci 133, jcs240341.
Liu B, Kilpatrick JI, Lukasz B, Jarvis SP, McDonnell F, Wallace DM, Clark AF, O'Brien CJ (2018). Increased substrate stiffness elicits a myofibroblastic phenotype in human lamina cribrosa cells. Invest Ophthalmol Vis Sci 59, 803–814.
Livne A, Geiger B (2016). The inner workings of stress fibers from contractile machinery to focal adhesions and back. J Cell Sci 129, 1293–1304.
Lo CM, Wang HB, Dembo M, Wang YL (2000). Cell movement is guided by the rigidity of the substrate. Biophys J 79, 144–152.
Mabuchi I, Okuno M (1977). The effect of myosin antibody on the division of starfish blastomeres. J Cell Biol 74, 251–263.
Machesky LM, Insall RH (1998). Scar1 and the related Wiskott–Aldrich syndrome protein, WASP, regulate the actin cytoskeleton through the Arp2/3 complex. Curr Biol 8, 1347–1356.
Mar PK, Roy P, Yin HL, Cavanagh HD, Jester JV (2001). Stress fiber formation is required for matrix reorganization in a corneal myofibroblast cell line. Exp Eye Res 72, 455–466.
Martino F, Perestrelo AR, Vinarský V, Pagliari S, Forte G (2018). Cellular mechanotransduction: from tension to function. Front Physiol 9, 824.
Masi I, Caprara V, Bagnato A, Rosanò L (2020). Tumor cellular and microenvironmental cues controlling invadopodia formation. Front Cell Dev Biol 8, 584181.
McNutt NS, Culp LA, Black PH (1971). Contact-inhibited revertant cell lines isolated from Sv40-transformed cells II. Ultrastructural study. J Cell Biol 50, 691–708.
Medalia O, Geiger B (2010). Frontiers of microscopy-based research into cell–matrix adhesions. Curr Opin Cell Biol 22, 659–668.
Mendes Pinto I, Rubinstein B, Kucharavy A, Unruh J, Li R (2012). Actin depolymerization drives actomyosin ring contraction during budding yeast cytokinesis. Dev Cell 22, 1247–1260.
Midgley AC, Woods EL, Jenkins RH, Brown C, Khalid U, Chavez R, Hascall V, Steadman R, Phillips AO, Meran S (2020). Hyaluronidase-2 regulates RhoA signaling, myofibroblast contractility, and other key profibrotic myofibroblast functions. Am J Pathol 190, 1236–1255.
Mochitate K, Pawelek P, Grinnell F (1991). Stress relaxation of contracted collagen gels: disruption of actin filament bundles, release of cell surface fibronectin, and down-regulation of DNA and protein synthesis. Exp Cell Res 193, 198–207.
Mogilner A, Oster G (1996). Cell motility driven by actin polymerization. Biophys J 71, 3030–3045.
Moustakas A, Stournaras C (1999). Regulation of actin organisation by TGF-beta in H-ras-transformed fibroblasts. J Cell Sci 112, 1169.
Muguruma M, Matsumura S, Fukazawa T (1990). Direct interactions between talin and actin. Biochem Biophys Res Commun 171, 1217–1223.
Mullins RD, Heuser JA, Pollard TD (1998). The interaction of Arp2/3 complex with actin: nucleation, high affinity pointed end capping, and formation of branching networks of filaments. Proc Natl Acad Sci USA 95, 6181–6186.
Mullins RD, Stafford WF, Pollard TD (1997). Structure, subunit topology, and actin-binding activity of the Arp2/3 complex from acanthamoeba. J Cell Biol 136, 331–343.
Murphy DA, Courtneidge SA (2011). The "ins" and "outs" of podosomes and invadopodia: characteristics, formation and function. Nat Rev Mol Cell Biol 12, 413–426.
Nakamura N, Oshiro N, Fukata Y, Amano M, Fukata M, Kuroda S, Matsuura Y, Leung T, Lim L, Kaibuchi K (2000). Phosphorylation of ERM proteins at filopodia induced by Cdc42. Genes Cells 5, 571–581.
Nasello G, Alamán-Díez P, Schiavi J, Pérez M,McNamara L, García-Aznar JM (2020). Primary human osteoblasts cultured in a 3D microenvironment create a unique representative model of their differentiation into osteocytes. Front Bioeng Biotechnol 8, 336.
Ní Annaidh A, Bruyère K, Destrade M, Gilchrist MD, Otténio M (2012). Characterization of the anisotropic mechanical properties of excised human skin. J Mech Behav Biomed Mater 5, 139–148.
Oelz D, Rubinstein B, Mogilner A (2015). A combination of actin treadmilling and cross-linking drives contraction of random actomyosin arrays. Biophys J 109, 1818–1829.
Pelham RJ, Chang F (2002). Actin dynamics in the contractile ring during cytokinesis in fission yeast. Nature 419, 82–86.
Pelham RJ, Wang YL (1997). Cell locomotion and focal adhesions are regulated by substrate flexibility. Proc Natl Acad Sci USA 94, 13661–13665.
Pelham RJ, Wang YL (1999). High resolution detection of mechanical forces exerted by locomoting fibroblasts on the substrate. Mol Biol Cell 10, 935–945.
Perdue JF (1973). The distribution, ultrastructure, and chemistry of microfilaments in cultured chick embryo fibroblasts. J Cell Biol 58, 265–283.
Powell K (2005). Myosin powers cytokinesis. J Cell Biol 170, 515.
Preibisch S, Saalfeld S, Tomancak P (2009). Globally optimal stitching of tiled 3D microscopic image acquisitions. Bioinformatics 25, 1463–1465.
Ridley AJ, Hall A (1992). The small GTP-binding protein rho regulates the assembly of focal adhesions and actin stress fibers in response to growth factors. Cell 70, 389–399.
Riedl J, Crevenna AH, Kessenbrock K, Yu JH, Neukirchen D, Bista M, Bradke F, Jenne D, Holak TA, Werb Z, *et al.* (2008). Lifeact: a versatile marker to visualize F-actin. Nat Methods 5, 605–607.
Rief M, Rock RS, Mehta AD, Mooseker MS, Cheney RE, Spudich JA (2000). Myosin-V stepping kinetics: a molecular model for processivity. Proc Natl Acad Sci USA 97, 9482–9486.
Rüegg C, Veigel C, Molloy JE, Schmitz S, Sparrow JC, Fink RHA (2002). Molecular motors: force and movement generated by single myosin II molecules. Physiology 17, 213–218.
Sandbo N, Lau A, Kach J, Ngam C, Yau D, Dulin NO (2011). Delayed stress fiber formation mediates pulmonary myofibroblast differentiation in response to TGF-β. Am J Physiol Lung Cell Mol Physiol 301, L656–L666.
Schell MJ, Erneux C, Irvine RF (2001). Inositol 1,4,5-trisphosphate 3-kinase A associates with F-actin and dendritic spines via its N terminus. J Biol Chem 276, 37537–37546
Seal A, Dalui AK, Banerjee M, Mukhopadhyay AK, Phani KK (2001). Mechanical properties of very thin cover slip glass disk. Bull Mater Sci 24, 151–155.
Shaner NC, Lambert GG, Chammas A, Ni Y, Cranfill PJ, Baird MA, Sell BR, Allen JR, Day RN, Israelsson M, *et al.* (2013). A bright monomeric green fluorescent protein derived from Branchiostoma lanceolatum. Nat Methods 10, 407–409.
Small J, Rottner K, Kaverina I, Anderson K (1998). Assembling an actin cytoskeleton for cell attachment and movement. Biochim Biophys Acta 1404, 271–281.
Small JV, Celis JE (1978). Filament arrangements in negatively stained cultured cells: the organization of actin. Cytobiologie 16, 308–325.
Solon J, Levental I, Sengupta K, Georges PC, Janmey PA (2007). Fibroblast adaptation and stiffness matching to soft elastic substrates. Biophys J 93, 4453–4461.
Subramanian D, Huang J, Sevugan M, Robinson RC, Balasubramanian MK, Tang X (2013). Insight into actin organization and function in cytokinesis from analysis of fission yeast mutants. Genetics 194, 435–446.
Suraneni P, Rubinstein B, Unruh JR, Durnin M, Hanein D, Li R (2012). The Arp2/3 complex is required for lamellipodia extension and directional fibroblast cell migration. J Cell Biol 197, 239–251.
Suzuki A, Itoh T (1993). Effects of calyculin A on tension and myosin phosphorylation in skinned smooth muscle of the rabbit mesenteric artery. Br J Pharmacol 109, 703–712.
Svitkina T (2018). The actin cytoskeleton and actin-based motility. Cold Spring Harb Perspect Biol 10, a018267.
Svitkina TM, Bulanova EA, Chaga OY, Vignjevic DM, Kojima SI, Vasiliev JM, Borisy GG (2003). Mechanism of filopodia initiation by reorganization of a dendritic network. J Cell Biol 160, 409–421.
Tee SY, Fu J, Chen C, Janmey P (2011). Cell shape and substrate rigidity both regulate cell stiffness. Biophys J 100, L25–L27.
Thoresen T, Lenz M, Gardel M (2011). Reconstitution of contractile actomyosin bundles. Biophys J 100, 2698–2705.
Tojkander S, Ciuba K, Lappalainen P (2018). CaMKK2 regulates mechanosensitive assembly of contractile actin stress fibers. Cell Rep 24, 11–19.
Tojkander S, Gateva G, Husain A, Krishnan R, Lappalainen P (2015). Generation of contractile actomyosin bundles depends on mechanosensitive actin filament assembly and disassembly. eLife 4, e06126.
Tomasek JJ, Gabbiani G, Hinz B, Chaponnier C, Brown RA (2002). Myofibroblasts and mechano-regulation of connective tissue remodelling. Nat Rev Mol Cell Biol 3, 349–363.

Tomasek JJ, Vaughan MB, Kropp BP, Gabbiani G, Martin MD, Haaksma CJ, Hinz B (2006). Contraction of myofibroblasts in granulation tissue is dependent on Rho/Rho kinase/myosin light chain phosphatase activity. Wound Repair Regen 14, 313–320.

Tosuji H (1992). Calyculin A induces contractile ring-like apparatus formation and condensation of chromosomes in unfertilized sea urchin eggs. Proc Natl Acad Sci USA 89, 10613–10617.

Turunen O, Wahlström T, Vaheri A (1994). Ezrin has a COOH-terminal actin-binding site that is conserved in the ezrin protein family. J Cell Biol 126, 1445–1453.

Uehata M, Ishizaki T, Satoh H, Ono T, Kawahara T, Morishita T, Tamakawa H, Yamagami K, Inui J, Maekawa M, Narumiya S (1997). Calcium sensitization of smooth muscle mediated by a Rho-associated protein kinase in hypertension. Nature 389, 990–994.

Verkhovsky AB, Borisy GG (1993). Non-sarcomeric mode of myosin II organization in the fibroblast lamellum. J Cell Biol 123, 637–652.

Vianay B, Senger F, Alamos S, Anjur-Dietrich M, Bearce E, Cheeseman B, Lee L, Théry M (2018). Variation in traction forces during cell cycle progression. Biol Cell 110, 91–96.

Vicente-Manzanares M, Ma X, Adelstein RS, Horwitz AR (2009). Non-muscle myosin II takes centre stage in cell adhesion and migration. Nat Rev Mol Cell Biol 10, 778–790.

Vignjevic D, Kojima SI, Aratyn Y, Danciu O, Svitkina T, Borisy GG (2006). Role of fascin in filopodial protrusion. J Cell Biol 174, 863–875.

Virtanen P, Gommers R, Oliphant TE, Haberland M, Reddy T, Cournapeau D, Burovski E, Peterson P, Weckesser W, Bright J, *et al*. (2020). SciPy 1.0: fundamental algorithms for scientific computing in Python. Nat Methods 17, 261–272.

Wang HB, Dembo M, Wang YL (2000). Substrate flexibility regulates growth and apoptosis of normal but not transformed cells. Am J Physiol Cell Physiol 279, C1345–C1350.

Wang Y, Riechmann V (2007). The role of the actomyosin cytoskeleton in coordination of tissue growth during Drosophila oogenesis. Curr Biol 17, 1349–1355.

Weber K, Groeschel-Stewart U (1974). Antibody to myosin: the specific visualization of myosin-containing filaments in nonmuscle cells. Proc Natl Acad Sci USA 71, 4561–4564.

Wegner A (1976). Head to tail polymerization of actin. J Mol Biol 108, 139–150.

Wei X, Henke VG, Strübing C, Brown EB, Clapham DE (2003). Real-time imaging of nuclear permeation by EGFP in single intact cells. Biophys J 84, 1317–1327.

Wong AJ, Pollard TD, Herman IM (1983). Actin filament stress fibers in vascular endothelial cells in vivo. Science 219, 867–869.

Wozniak MA, Chen CS (2009). Mechanotransduction in development: a growing role for contractility. Nat Rev Mol Cell Biol 10, 34–43.

Wu C, Asokan S, Berginski M, Haynes E, Sharpless N, Griffith J, Gomez S, Bear J (2012). Arp2/3 is critical for lamellipodia and response to extracellular matrix cues but is dispensable for chemotaxis. Cell 148, 973–987.

Zaman MH, Trapani LM, Sieminski AL, MacKellar D, Gong H, Kamm RD, Wells A, Lauffenburger DA, Matsudaira P (2006). Migration of tumor cells in 3D matrices is governed by matrix stiffness along with cell-matrix adhesion and proteolysis. Proc Natl Acad Sci USA 103, 10889–10894.

Zhou DW, Lee TT, Weng S, Fu J, García AJ (2017). Effects of substrate stiffness and actomyosin contractility on coupling between force transmission and vinculin–paxillin recruitment at single focal adhesions. Mol Biol Cell 28, 1901–1911.

Zhou M, Wang YL (2008). Distinct pathways for the early recruitment of myosin II and actin to the cytokinetic furrow. Mol Biol Cell 19, 318–326..

Zhu W, Castro NJ, Cui H, Zhou X, Boualam B, McGrane R, Glazer RI, Zhang LG (2016). A 3D printed nano bone matrix for characterization of breast cancer cell and osteoblast interactions. Nanotechnology 27, 315103.